Single-cell atlas of hepatitis C virus inoculated tree shrew liver reveals immune activation, metabolic reprogramming, and persistent inflammation

Dandan Yu,[a,b,c,g] Wei-Bo Kang,[a,c,g] Yu-Hua Ma,[b] Long-Bao Lv,[b] Shihua Zhang,[d] Lei Tang,[e] Sheng Liu,[e] Jin Zhong,[f,**] and Yong-Gang Yao[a,b,c,*]

[a]State Key Laboratory of Genetic Evolution and Animal Models, Key Laboratory of Animal Models and Human Disease Mechanisms of Yunnan Province, Yunnan Engineering Center on Brain Disease Models, and KIZ-CUHK Joint Laboratory of Bioresources and Molecular Research in Common Diseases, Kunming Institute of Zoology, Chinese Academy of Sciences, Kunming, Yunnan 650201, China
[b]National Resource Center for Non-Human Primates, National Research Facility for Phenotypic & Genetic Analysis of Model Animals (Primate Facility), Kunming Institute of Zoology, Chinese Academy of Sciences, Kunming, Yunnan 650107, China
[c]Kunming College of Life Science, University of Chinese Academy of Sciences, Kunming, Yunnan 650204, China
[d]State Key Laboratory of Mathematical Sciences, Academy of Mathematics and Systems Science, Chinese Academy of Sciences, Beijing 100190, China
[e]State Key Laboratory of Ophthalmology, Zhongshan Ophthalmic Center, Sun Yat-sen University, Guangdong Provincial Key Laboratory of Ophthalmology and Visual Science, Guangdong Province Key Laboratory of Brain Function and Disease, Guangzhou 510623, China
[f]Shanghai Institute of Immunity and Infection, Shanghai Institute of Materia Medica, Chinese Academy of Sciences, Shanghai 200031, China

eBioMedicine
2026;123: 106080
Published Online xxx
https://doi.org/10.1016/j.ebiom.2025.106080

Summary

Background Hepatitis C virus (HCV) remains a major global health challenge, largely due to the absence of robust animal models that recapitulate this disease, hindering mechanistic studies and vaccine development. This study employed tree shrews to determine the molecular profiles of distinct liver cell populations following HCV infection.

Methods Tree shrews received intrahepatic injections of the HCV JFH1 strain and were analysed at two timepoints: 1 week post-inoculation (acute) and 111 weeks post-inoculation (long-term). Viral load was assessed up to 30 weeks. Liver pathology was assessed via haematoxylin and eosin (H&E) staining. Single-cell transcriptomic profiling was performed on liver tissues, while tree shrew primary hepatocytes and ITH6 hepatic cells, as well as human Huh7 cells, were used to characterise cellular changes following HCV infection.

Findings Sixteen major cell types were identified in 157,298 liver cells across HCV-inoculated and control tree shrews. Acute inoculation triggered widespread induction of interferon-stimulated genes (ISGs) across all cell types, including the periportal ISG^{high} hepatocyte subcluster, and concurrent reduction in metabolic gene expression in hepatocytes *in vivo*. Impaired glucose metabolism, as confirmed in HCV-exposed ITH6 cells, likely contributed to this metabolic shift. Erythroblasts were exclusively detected during acute inoculation and exhibited enhanced intercellular communication signatures. Among neutrophils, three distinct subclusters were identified, one of which displayed elevated expression of neutrophil extracellular trap (NET) markers and enhanced NET formation in inoculated livers.

Interpretation This study provides a comprehensive single-cell transcriptomic landscape of HCV-inoculated tree shrew livers. These findings underscore the use of the tree shrew model for advancing mechanistic understanding of HCV pathogenesis, as well as its relevance for therapeutic and vaccine development.

Funding This work was supported by grants from National Natural Science Foundation of China (U1902215, U25A20646), National Key Research and Development Plan Program (2022YFF0710900), Key Project of the CAS "Light of West China" Program (xbzg-zdsys-202302), and Yunnan Province (202305AH340006, 202001AS070023).

*Corresponding author. State Key Laboratory of Genetic Evolution and Animal Models, Key Laboratory of Animal Models and Human Disease Mechanisms of Yunnan Province, Yunnan Engineering Center on Brain Disease Models, and KIZ-CUHK Joint Laboratory of Bioresources and Molecular Research in Common Diseases, Kunming Institute of Zoology, Chinese Academy of Sciences, Kunming, Yunnan 650201, China
**Corresponding author.
E-mail addresses: yaoyg@mail.kiz.ac.cn (Y.-G. Yao), jzhong@ips.ac.cn (J. Zhong).
[g]These authors contributed equally.

Keywords: HCV; Chinese tree shrew; Single-cell RNA sequencing; Hepatocytes; Erythroblasts; Neutrophils

Research in context

Evidence before this study

Research on the immune microenvironment of HCV-infected individuals remains scarce. Although some studies have characterised the immune features of peripheral T cells and hepatic myeloid cells throughout direct-acting antiviral (DAA) therapy using single-cell sequencing, these investigations have primarily focused on the chronic phase or post-treatment. In contrast, the tree shrew model enabled longitudinal characterisation of intrahepatic immunity across both acute and extended phases of inoculation, thereby bridging a critical gap in early-stage HCV pathogenesis.

Added value of this study

This study utilised tree shrews to map the single-cell transcriptional landscape of liver cells during acute and chronic HCV inoculation. Key findings demonstrate that acute inoculation triggers a broad interferon response, metabolic reprogramming in hepatocytes, and the emergence of functionally distinct immune subsets—including immunomodulatory erythroblasts and enhanced NET formation in neutrophils.

Implications of all the available evidence

By mapping early host-pathogen interactions, this work provides a foundational resource for understanding HCV-induced liver injury. These findings provide new insights into how HCV affects liver cells during early infection. The tree shrew model offers a practical system for studying HCV mechanisms and testing potential treatments, complementing existing research tools.

Introduction

Hepatitis C virus (HCV) infection constitutes a persistent global health burden. Over 50 million individuals suffer chronic infection worldwide, leading to approximately 240,000 deaths and a million new infections each year.[1] However, true prevalence is likely underestimated, as actual case numbers are predicted to be nearly twice the number of confirmed cases.[2] HCV infection is frequently asymptomatic during the acute phase, facilitating undetected viral persistence, with 75%–80% of cases ultimately progressing to chronic infection.[3] Over time, this persistent viral presence can culminate in progressive liver pathology, including fibrosis, cirrhosis, and hepatocellular carcinoma.[4] While the introduction of direct-acting antiviral agents (DAAs) has markedly improved therapeutic outcomes, achieving sustained virologic response rates exceeding 95%,[5] most HCV-infected individuals remain undiagnosed and untreated.[6] As such, HCV infection continues to be a leading cause of liver-related morbidity and mortality. A comprehensive approach combining antiviral therapy with vaccination represents the most promising strategy for HCV eradication. To date, however, no effective prophylactic or therapeutic vaccine has been successfully developed.[7] This limitation largely reflects an incomplete understanding of HCV pathogenesis and host immune dynamics, further compounded by the absence of a suitable animal model for evaluating vaccine efficacy.[8]

The host tropism of HCV is remarkably restricted, with natural susceptibility observed only in humans and chimpanzees.[9] While chimpanzee models were instrumental in elucidating viral pathogenesis and advancing preclinical trials,[9] their use has been globally prohibited due to ethical constraints. Consequently, alternative models have since been explored, including genetically modified and human liver-chimeric mice, which exhibit partial susceptibility to HCV.[8] However, the profound genetic and immunological differences between mice and humans also result in significant disparities in pathological responses following HCV infection, limiting their translational relevance.[10] In contrast, tree shrews (*Tupaia belangeri*), small, squirrel-like mammals more closely related to primates than to rodents,[11–13] have emerged as a promising and permissive non-primate model for HCV infection.[14–19] Multiple studies have demonstrated that tree shrews express functional orthologs of HCV entry factors,[16,20,21] enabling viral entry into primary hepatocytes.[14,15,21,22] HCV infection in tree shrews can persist over time and has been associated with progressive liver pathology, including steatosis, fibrosis, and hepatocellular carcinoma.[19] Nonetheless, most HCV-infected tree shrews exhibit intermittent viraemia with low viral load and fail to sustain robust, long-term infection.[19,23] Thus, HCV infection in tree shrews remains inefficient and inconsistent, hindering its utility for clarifying the mechanism of viral persistence, viral clearance, immune evasion, and vaccine-induced protection.

The liver, the primary target organ of HCV replication, comprises a complex cellular ecosystem, including hepatocytes, sinusoidal endothelial cells, and a wide array of resident and infiltrating immune cells, which collectively function to maintain hepatic homeostasis and orchestrate responses to pathological insults.[24,25] Upon HCV infection, this dynamic microenvironment

undergoes immune activation characterised by the recruitment of diverse immune cell subtypes.[26] However, the cellular complexity of the liver poses substantial challenges in identifying the precise roles of specific immune populations during HCV pathogenesis.[27] Advances in single-cell RNA sequencing (scRNA-seq) have enabled high-resolution mapping of hepatic cellular heterogeneity under physiological and disease conditions.[24,28–30] Recent studies have provided critical insights into the composition and function of liver-resident myeloid cells, including neutrophils, eosinophils, mast cells, basophils, dendritic cells, and monocytes/macrophages, in individuals with chronic HCV infection of following viral clearance.[31] Nevertheless, the majority of available liver tissue samples originate from patients with established chronic disease, limiting the capacity to investigate early immunological events following HCV exposure. The lack of access to tissue at defined early timepoints, due to the asymptomatic nature and unknown onset of infection in humans, continues to impede efforts to delineate cell type-specific antiviral responses at disease onset.

In this context, experimental infection of tree shrews offers a unique opportunity to capture early-stage host responses in a controlled setting. Here, HCV infection was established in tree shrews by intrahepatic delivery of HCV genomic RNA. Liver tissues were harvested following both acute and long-term inoculation and subjected to scRNA-seq and single-nucleus RNA-seq (snRNA-seq). This approach enabled construction of a comprehensive single-cell atlas and delineation of transcriptional dynamics across major hepatic cell populations following HCV challenge. Notably, hepatocytes, erythroblasts, and neutrophils exhibited pronounced alterations in gene expression and intercellular communication networks upon HCV inoculation. These findings provide a valuable resource for understanding early liver immune responses to HCV and underscore the relevance of the tree shrew as a tractable model for studying viral hepatitis.

Methods

Animals

A total of 39 Chinese tree shrews were obtained from the experimental animal centre of the Kunming Institute of Zoology, Chinese Academy of Sciences. Detailed information about these animals is listed in Supplementary Table S1. The tree shrews were acclimated for 1 week before treatment. All treated animals were housed at the Animal Biosafety Level 2 Laboratory (ABSL-2) of the Kunming Institute of Zoology on a 12-h light/dark cycle, with free access to food and water. All animal experiments were conducted in compliance with the Animal Ethics Committee of the Kunming Institute of Zoology, Chinese Academy of Sciences (Approval number: SMKX-20190310-42). The viral infection experiments were performed using age-matched female tree shrews.

HCV RNA synthesis

The pUC-vJFH1 plasmid was linearised with *Xba*I (FD0684, Thermo Fisher), extracted with phenol and chloroform, precipitated with ethanol, and dissolved in RNase-free water. The linearised plasmid was used for *in vitro* RNA transcription with the MEGAscript T7 transcription kit (AM1334, Thermo Fisher) following the manufacturer's protocols. In brief, 20 μL of reaction transcription mixture containing 1 μg of linearised plasmid, 1× reaction buffer, 2 μL of each ribonucleotide solution (75 mM), and 2 μL of T7 enzyme mix were incubated at 37 °C for 4 h. Synthetic RNA was treated with 2 U DNase to remove template DNA. The synthesised RNA was purified by phenol/chloroform and isopropanol precipitation, and RNA purity and concentration were determined using a spectrophotometer. RNA integrity was checked by agarose gel electrophoresis. RNA (10 μg or 30 μg) was diluted in 200 μL of phosphate-buffered saline (PBS) and stored at –80 °C until intrahepatic inoculation.

Virus inoculation

Before inoculation, all animals were confirmed HCV-negative via RT-PCR (see below). For inoculation, the tree shrews were anesthetised intramuscularly with ketamine (50 mg/mL, 50 mg/kg) and pentobarbital (30 mg/mL, 60 mg/kg). Under aseptic conditions, the abdomen was opened to expose the left hepatic lobe. HCV RNA (10 μg or 30 μg) dissolved in 200 μL of PBS was injected into three separate sites within the liver using an insulin needle. Injection was visually confirmed by transient blanching of the tissue, followed by gradual reperfusion. The needle was withdrawn slowly, and pressure was immediately applied with a sterile cotton swab to control bleeding. The abdominal wall and skin were sutured, and animals were closely monitored until full recovery. For animals followed to 111 wpi, weekly blood samples (800 μL) were collected via venipuncture, and serum was isolated by centrifugation at 2000 *g* for 15 min at room temperature and stored at –80 °C for HCV RNA quantification.

To evaluate whether hepatic ISG zonation and the emergence of erythroblast could be induced by other viral stimuli or IFNα treatment, additional tree shrews were intravenously inoculated with green fluorescent protein (GFP)-tagged vesicular stomatitis virus (VSV-GFP),[32] adeno-associated virus serotype 8 expressing mCherry (AAV8-mCherry) under different promoters (AAV8.TBG.mCherry.WPRE.SV40pA and AAV8.CAG.mCherry.WPRE.SV40pA, PackGene Biotech), or universal type I IFN (11200-2, PBL Assay Science). Five animals received 1×10^9 PFU of VSV-GFP and were euthanised at 3 or 7 days post-infection (dpi); control animals received no virus and were euthanised in

parallel ($n = 2–3$ animals per group). Two tree shrews were infected with AAV8-mCherry virus (1×10^{12} genome copies) and sacrificed at 4 weeks post-inoculation (wpi), alongside a PBS-injected control. Four animals were treated with universal type I IFN (2×10^5 units) and sacrificed at 8 or 24 h post-injection (hpi), alongside two PBS-injected controls (Supplementary Table S1).

All animals were housed under ABSL-2 conditions with a 12-h light/dark cycle and *ad libitum* access to food and water. Sacrifice was performed at designated timepoints under approved ethical protocols.

Tissue acquisition, dissociation, and preparation

Following the above anaesthesia methods, tree shrews were intracardially perfused with ice-cold PBS. The left hepatic lobe was promptly excised and sectioned into six equal portions on ice. Two portions were processed for scRNA-seq and snRNA-seq, one portion was used for bulk RNA-seq, and one portion was fixed in 4% paraformaldehyde (PFA) in PBS for histopathological staining. The remaining tissue was snap-frozen and stored at –80 °C for subsequent viral load and gene expression quantification.

For scRNA-seq, freshly excised liver samples were immediately immersed in Tissue Preservation Solution (Singleron Biotechnologies, China) and stored at 2–8 °C. Approximately 100 mg of tissue was washed three times with Hanks' Balanced Salt Solution (HBSS), minced into 1–2 mm pieces, and enzymatically digested in 2 mL of Liver Tissue Dissociation Solution (Singleron Biotechnologies, China) at 37 °C under continuous agitation for 15 min. The resulting cell suspension was passed through a 70-μm sterile strainer to remove debris and centrifuged at 350 *g* for 5 min at 4 °C. Cell pellets were resuspended in 1 mL of PBS (HyClone), and red blood cells were lysed using GEXSCOPE Red Blood Cell Lysis Buffer (Singleron Biotechnologies, China) for 5 min at room temperature. After a second centrifugation at 300 *g* for 5 min at 4 °C, the remaining cells were resuspended in PBS. Cell viability was assessed via trypan blue staining (Sigma) under a phase-contrast microscope (Nikon, Japan). Viable cells were counted using a TC20 automated cell counter (Bio-Rad) and the concentration was adjusted to 1×10^5 cells/mL in PBS.

For snRNA-seq, liver samples were snap-frozen in liquid nitrogen and stored at –80 °C. Nuclei were isolated by washing frozen tissue in ice-cold PBSE (PBS buffer containing 2 mM EGTA) and processed using GEXSCOPE Nucleus Separation Solution (Singleron Biotechnologies, China) according to the manufacturer's manual. Isolated nuclei were resuspended in PBSE to a final concentration of 10^6 nuclei per 400 μL, filtered through a 40-μm cell strainer, and stained with 4′,6-diamidino-2-phenylindole (DAPI, D1306, Thermo Fisher). DAPI-positive singlets were used for downstream processing.

To analyse erythroid genes expression in foetal tree shrew liver tissues, pregnant tree shrews were obtained from the experimental animal centre of the Kunming Institute of Zoology, Chinese Academy of Sciences to collect foetus. Briefly, pregnant tree shrews at defined timepoints were euthanised following the above procedure. Foetuses at embryonic day (E) 26 to E37 were collected, and foetal liver tissues were harvested, washed in ice-cold PBS, and stored at –80 °C until use.

RNA sequencing (RNA-seq) for bulk tissues and cells

Total RNA was isolated from bulk liver tissues and cultured cells using TRIzol reagent (15596018CN, Thermo Fisher). Downstream quality control, library construction, and sequencing were performed by Novogene Co., Ltd. (Beijing, China). Raw sequencing data were processed with TrimGalore v0.6.10 (https://github.com/FelixKrueger/TrimGalore) for adapter trimming and quality. Cleaned reads were aligned to the tree shrew reference genome TS_3.0 (https://www.treeshrewdb.org) using STAR v2.7.10b (https://github.com/alexdobin/STAR/releases).[33] Gene- and transcript-level quantification was performed using RSEM v1.3.3 (https://github.com/deweylab/RSEM). Gene-level expression matrices from all samples were merged using rsem-generate-data-matrix, and differential expression analysis was conducted with DESeq2 (v1.38.3),[34] with differentially expressed genes (DEGs) defined by a threshold of $|\log_2 (\text{fold change})| > 1$ and Benjamini-Hochberg's (BH) adjusted P (FDR) < 0.05.

To investigate the transcriptional response of primary human hepatocytes (PHHs) to HCV infection, we (re-)analysed RNA-seq data of PHHs from three donors (GEO, accession number GSE132548). In this dataset, PHHs were either mock-infected or HCV-infected (1 MOI), and harvested at 6 or 72 h post-infection for RNA-seq.

Preparation of single-cell sequencing libraries

Single-cell suspensions (2×10^5 cells/mL in PBS, HyClone, USA) were loaded into microfluidic devices using the Singleron Matrix® Single Cell Processing System (Singleron Biotechnologies, China). Subsequently, scRNA-seq and snRNA-seq libraries were established using the GEXSCOPE® Single Cell RNA Library Kit and GEXSCOPE® Single Nucleus RNA Library Kit (Singleron Biotechnologies, China), respectively. Libraries were normalised to 4 nM, pooled, and sequenced on the Illumina NovaSeq 6000 platform with 150 bp paired-end reads.

Read processing and expression quantification

Raw sequencing data were processed to generate gene expression matrices using the CeleScope v1.14.1 pipeline (https://github.com/singleron-RD/CeleScope). Reads were first filtered using Cutadapt v3.7 (https://

github.com/marcelm/cutadapt)[35] to remove low-quality reads, poly-A tails, and adapter sequences. Cell barcodes and unique molecular identifiers (UMIs) were extracted, and reads were mapped to the reference genome TS_3.0 (https://www.treeshrewdb.org)[13,36] using STAR v2.6.1a (https://github.com/alexdobin/STAR).[33] UMI and gene counts for each cell were performed using featureCounts v2.0.1 (https://subread.sourceforge.net/featureCounts.html)[37] and used to generate expression matrix files for subsequent analysis.

Quality control and single-cell clustering

Single-cell RNA sequencing data were processed and quality-controlled using Scanpy v1.9.8 (https://github.com/scverse/scanpy).[38] Fourteen expression matrices were analysed in total. Potential doublets were computationally predicted using Scrublet (https://github.com/swolock/scrublet).[39] To mitigate batch effects across multiple samples, principal component analysis (PCA) was performed on the normalised expression matrix, followed by data integration using Harmony (https://github.com/immunogenomics/harmony). The integrated low-dimensional embeddings were then utilised for subsequent non-linear dimensionality reduction via Uniform Manifold Approximation and Projection (UMAP). To improve cluster resolution, each primary cluster underwent iterative re-clustering, as described in the previous research.[40] Briefly, for each round of sub-clustering, a nearest-neighbour graph was computed based on the integrated Harmony-corrected principal components, followed by graph-based clustering. Subclusters with elevated doublet scores or aberrant transcriptomic profiles (e.g., extreme numbers of detected genes) were excluded. Following this stringent filtering process, 16 distinct cell populations were delineated and integrated for downstream analyses.

DEG analysis and cell type annotation

DEGs for each cell population were identified using the *rank_genes_groups* function in Scanpy,[38] with statistical significance assessed using the Wilcoxon rank-sum test, followed by BH correction for multiple hypothesis testing to determine FDR. Cell type annotation was subsequently conducted by cross-referencing the expression profiles of DEGs with established marker genes from the Liver Cell Atlas (https://www.livercellatlas.org/),[41] ensuring accurate and biologically meaningful classification of the identified cell populations.

Pathway enrichment analysis and gene module scoring

To elucidate the biological significance of the identified DEGs ($\log_2$ (fold change) > 0.5, FDR < 10^{-5}, keeping all (when <500 genes) or the top 500 most significant genes), functional enrichment analysis was performed using Metascape (https://metascape.org/).[42] DEGs were mapped to human Gene Ontology (GO) terms and pathways. Gene Set Variation Analysis (GSVA) was carried out using ReactomeGSA (https://github.com/reactome/ReactomeGSA),[43] enabling pathway-centric analysis of single-cell transcriptomic data by projecting gene expression profiles onto the Reactome database.[43] Enrichment scores were computed per cell, and visualisations were generated using the ggplot2 package in R. Additionally, gene module activity was assessed using the *score_genes* function in Scanpy[38] to calculate average expression scores for predefined gene sets at single-cell resolution.

Cell-cell interaction analysis

To characterise intercellular communication dynamics during the acute phase of HCV RNA exposure, CellPhoneDB (https://github.com/ventolab/CellphoneDB)[44] was used to analyse ligand-receptor interactions at single-cell resolution. Analysis was performed by integrating single-cell transcriptomic data with the curated database of ligand-receptor pairs, enabling the identification and quantification of statistically significant cell-cell interactions ($P < 0.05$) based on co-expression patterns of interacting molecules. To visualise the complex interaction networks, ktplots (https://github.com/zktuong/ktplots) was utilised, providing detailed graphical representations of cell-type-specific signalling relationships.

Cross-species comparative analysis

To investigate the developmental origins and conserved characteristics of hepatic erythroblasts, erythroblasts from tree shrew livers following acute HCV inoculation were integrated with erythroid subsets, including proerythroblasts, erythroblasts, and erythrocytes, from mouse livers at postnatal days 1, 3, 7, 21, and 56.[45] The Batch Balanced K-Nearest Neighbour (BBKNN) algorithm (https://github.com/Teichlab/bbknn)[46] was applied to eliminate batch effects introduced by species-specific and technical variability, revealing the underlying cellular relationships.

Trajectory analysis

To delineate cellular differentiation trajectories and identify key regulatory genes, pseudotime analysis was performed using monocle3 (https://github.com/cole-trapnell-lab/monocle3).[47] A high-dimensional trajectory model was constructed based on the transcriptional profiles of individual cells. Cells were ordered along a continuous manifold based on transcriptional similarity, capturing differentiation dynamics at single-cell resolution. Genes exhibiting significant expression changes along pseudotime were identified as candidate regulators of lineage progression. ClusterGVis (https://github.com/junjunlab/ClusterGVis) was used to

visualise and interpret these gene expression dynamics across inferred trajectories.

Quantification of viral RNA and serum glucose

Viral RNA was extracted from 200 μL of tree shrew serum using a TIANamp Virus RNA Kit (DP315, TIANGEN). Total RNA from liver tissue homogenates was isolated with TRIzol reagent (15596018CN, Thermo Fisher). For HCV RNA quantification, 10 μL of RNA was subjected to a one-step real-time RT-PCR assay using the THUNDERBIRD Probe One-step qRT-PCR Kit (QRZ-101, TOYOBO) following the manufacturer's instructions. Primer and probe sequences for HCV RNA detection are listed in Supplementary Table S2. Standard curves generated from standard dilutions of RNA standards were used to calculate viral copy numbers. Serum glucose and alanine aminotransferase (ALT) levels were determined using the Dimension® EXL™ 200 Integrated Chemistry System (Siemens).

Histological and immunostaining analyses

Liver tissues were collected from anaesthetised tree shrews via abdominal incision, fixed in 4% PFA, embedded in paraffin, sectioned at 4 μm, and stained with haematoxylin and eosin (H&E). Immunohistochemical staining followed established protocols.[48,49] Tissue sections were baked at 65 °C for 30 min, deparaffinised using buffer (G1128, Servicebio), and subsequently rehydrated through a graded ethanol series (100%–50%). Heat-induced antigen retrieval was performed using sodium citrate buffer (pH 6.0) (MVS-0101, MXB Biotechnologies). Endogenous peroxidase activity was quenched with 3% hydrogen peroxide for 25 min (only for immunohistochemical analysis), and non-specific binding was blocked with 5% bovine serum albumin (BSA, B824162, Macklin) for 30 min at room temperature. Sections were incubated overnight at 4 °C with rabbit anti-AHSP antibody (1:300, GB111822, Servicebio). Negative controls were incubated with rabbit immunoglobulin G (IgG) (GB23303, Servicebio). Immunoreactivity was visualised using 3,3′-diaminobenzidine tetrahydrochloride (DAB) and imaged under an Olympus OlyVIA microscope (Japan).

For immunofluorescence staining, heat-induced antigen retrieval was performed using sodium citrate buffer (pH 6.0) or Tris-EDTA (pH 9.0) (G1203, Servicebio). Sections were incubated with primary antibodies (Supplementary Table S3) overnight at 4 °C, followed by corresponding secondary antibody (Supplementary Table S3) incubation for 1 h at room temperature. All antibodies were validated by the respective manufacturers and/or us. The slides were stained with DAPI (MB3204, Meilunbio) for 20 min to label cell nuclei, then sealed with anti-fluorescence quenching sealing agent (Fluoromount-G, 0100-01, SouthernBiotech) and imaged at 20× magnification using the TissueGnostics system. Immunofluorescence signal intensities were quantified using ImageJ software.

Cell culture, viral infection, and chemical treatments

ITH6 cells were cultured according to our previous report.[50] Primary tree shrew hepatocytes (PTHs) were isolated from healthy adult animals using established procedures.[22,51] Huh7 cells were obtained from the Kunming Cell Bank (Kunming Institute of Zoology, Chinese Academy of Sciences) and cultured in high-glucose Dulbecco's Modified Eagle Medium (DMEM, 11965-092, Thermo Fisher) supplemented with 10% foetal bovine serum (FBS, LONSERA, S711-001) and 1× penicillin/streptomycin (15140122, Thermo Fisher) at 37 °C in 5% CO_2. Galactose-based DMEM was prepared using glucose-free DMEM (11966-025, Thermo Fisher) supplemented with 10% FBS, 10 mM galactose (G5388, MERCK), 5 mM HEPES (H9136, MERCK), and 1× penicillin/streptomycin. Cells were routinely tested and confirmed to be free of mycoplasma contamination by PCR assay.

The preparation and titration of EGFP-tagged HCV followed our previous studies.[22,51] For infection assays, cells were exposed to virus at two multiplicities of infection (MOIs = 0.1 or 0.4) for 6 h, followed by two washes with PBS and replacement with fresh medium. Samples of cells and culture media were collected at indicated timepoints. For glycolysis inhibition, cells were treated with either 2 mM 2-deoxy-D-glucose (2-DG; HY-13966, MedChemExpress) or R-GEN-140 (5 or 15 μM; HY-100742A, MedChemExpress) following the 6 h infection period, and incubated under these conditions until harvest.

Quantification of glucose and lactic acid levels

Culture media from ITH6 to Huh7 cells under various treatment conditions were collected and analyzed for glucose and lactic acid concentrations using a Glucose Assay Kit with O-toluidine (S0201M, Beyotime Biotechnology) and a L-Lactic Acid Content Assay Kit (BC2235, Solarbio) according to the manufacturer's instructions.

Quantitative RT-PCR (qRT-PCR)

Total RNA was extracted from cultured cells using TRIzol reagent (15596018CN, Thermo Fisher) according to the manufacturer's instructions. cDNA was synthesised using M-MLV reverse transcriptase (M1701, Promega) with a mixture of Oligo (dT) and random primers. qRT-PCR was performed using iTaq Universal SYBRGreen Supermix (1725124, Bio-Rad) and gene-specific primers (Supplementary Table S2) on the CFX Connect Real-Time System (Bio-Rad). The reaction mixture was denatured at 95 °C for 30 s, followed by 40 cycles at 95 °C 5 s and 60 °C 30 s. The

mRNA levels of the selected genes were normalised to β-actin, and relative fold changes were calculated using the $2^{-\Delta\Delta Ct}$ method.[52]

Western blotting

Protein extraction and western blotting were performed as previously described.[22,32,50] Liver tissues and cells were lysed with RIPA lysis buffer (P0013C, Beyotime Biotechnology), and total protein concentrations were determined using a BCA Protein Assay Kit (P0012, Beyotime Biotechnology). Equal amounts of protein (25 μg) were separated by 12% sodium dodecyl sulphate-polyacrylamide gel electrophoresis (SDS-PAGE) and transferred to polyvinylidene fluoride (PVDF) membranes (1620177, Bio-Rad). The membranes were blocked with 5% (w/v) skim milk or 5% BSA in Tris-buffered saline containing 0.1% Tween 20 (TBST) and incubated overnight at 4 °C with appropriate primary antibodies (Supplementary Table S3). After three washes with TBST (5 min each), the membranes were incubated with the corresponding secondary antibodies (Supplementary Table S3) for 1 h at room temperature. Protein bands were visualised using an ultrasensitive ECL Detection Kit (PK10003, Proteintech) on the ChemiDoc MP imaging system (Bio-Rad).

Statistical analysis

For the scRNA-seq and snRNA-seq data, we used the default setting of Scanpy v1.9.8 (https://github.com/scverse/scanpy)[38] for identifying DEGs and comparing differences between two groups. The Wilcoxon rank-sum test (for a non-parametric data and deviations from normality) was applied to identify DEGs (FDR < 10^{-5}) in each cluster and difference between the two experimental groups. For comparisons involving three groups, we first used the Kruskal-Wallis test (a non-parametric alternative to ANOVA) to assess overall differences, followed by Dunnett's multiple comparisons test.

To quantify differences among different groups in animal and/or cellular experiments, we first tested the normality of the data using the Shapiro-Wilk test. For non-normally distributed data, the Mann-Whitney test was used. For datasets passing the normality test ($P > 0.05$), we performed an unpaired two-tailed Student's *t*-test to discern difference between two groups. For cases where parametric tests were justified (normally distributed data), we explicitly used one-way analysis of variance (ANOVA) with Tukey's post-hoc test for multiple comparisons to assess differences among three or more groups. For time-course gene expression assays in cultured cells, measurements at each time point (24 h, 48 h, and/or 72 h) were taken from independent wells ($n = 3$ wells per group per time point in a 12-well plate). Data were presented as mean ± standard deviation (SD) and analyzed using a two-way ANOVA with *treatment* (control group, 0.1 MOI group, 0.4 MOI group) and *time* as independent factors, followed by Tukey's multiple comparisons test. Statistical analyses were performed using GraphPad Prism v10.1. A P value < 0.05 was considered statistically significant.

Role of funders

The funders of this study had no role in study design, sample collection, data collection, data analyses, interpretation, or writing of the report.

Results

Dynamics of serum HCV RNA following intrahepatic inoculation in tree shrews

To assess the capacity of intrahepatic HCV RNA delivery to establish infection in tree shrews, a method previously validated in chimpanzees[53–55] and chimeric mice,[56] *in vitro*-transcribed HCV RNA (JFH1 strain)[57] or PBS (control) was injected into the liver of 18 animals. The tree shrews were assigned into acute (1 week) and long-term (111 weeks) groups. The acute group comprised PBS-S controls ($n = 6$) and JFH1-S animals receiving 30 μg of HCV RNA ($n = 6$), while the long-term group included PBS-L ($n = 2$), JFH1-LL (10 μg HCV RNA, $n = 2$), and JFH1-LH (30 μg HCV RNA, $n = 2$) animals (Fig. 1A and Supplementary Table S1).

Serum HCV RNA levels were quantified weekly post-inoculation using TaqMan probe-based one-step qRT-PCR. Viral RNA became detectable in several inoculated animals within the first few weeks (Supplementary Fig. S1a). Notably, tree shrew JFH1-LH_20 exhibited 10^2 copies/mL at 2 weeks post-inoculation (2 wpi), which increased to 10^4 copies/mL by 8 wpi. Although viral RNA was detected intermittently or persistently in all HCV-inoculated animals, serum HCV levels generally declined over time and were largely undetectable beyond 28 wpi. However, this finding was limited to observations in four tree shrews. At 111 wpi, no HCV RNA was detectable in hepatic tissues of any animal. Histopathological analyses were performed on liver tissues from both HCV-inoculated and PBS-treated tree shrews. At 1 wpi, livers (JFH1-S_51 and JFH1-S_52) exhibited immune cell infiltration and extramedullary haematopoiesis compared to PBS-treated controls. By 111 wpi, animals (JFH1-LL_16 and JFH1-LH_21) demonstrated progression to hepatic steatosis accompanied by persistent immune cell infiltration (Supplementary Fig. S1b).

Single-cell transcriptomic profiling of hepatic cells in tree shrew liver

To dissect the cellular landscape and transcriptional architecture of tree shrew livers during HCV inoculation, liver tissues were harvested from ten individuals representing both early (1 wpi) and late (111 wpi)

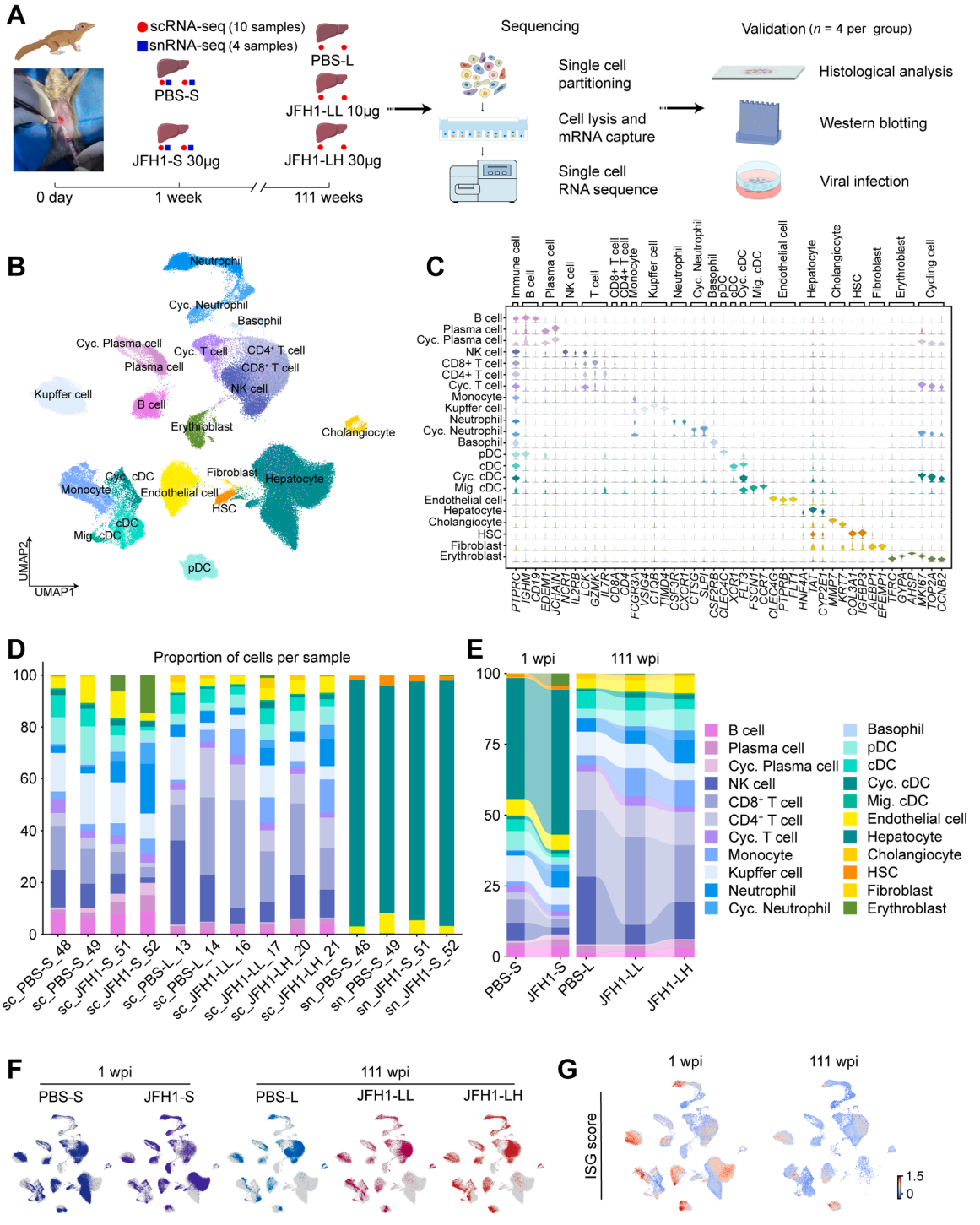

***Fig. 1:* Single-cell transcriptional landscape of hepatic cells in HCV-inoculated tree shrews.** (A) Schematic overview of study design. Liver samples were collected from tree shrews at acute (1 week post-HCV RNA inoculation, 1 wpi; JFH1-S group, 30 μg HCV RNA) and long-term (111 weeks post-inoculation, 111 wpi; JFH1-LL group, 10 μg HCV RNA; JFH1-LH group, 30 μg HCV RNA) stages, along with PBS-injected controls. scRNA-seq (n = 10 samples) and snRNA-seq (n = 4 samples) were conducted for transcriptomic profiling. Detailed sample information is listed in Supplementary Table S1. (B) UMAP visualisation of cell types identified in liver samples from tree shrews at 1 wpi and 111 wpi. Each dot represents a single cell. Cyc., cycling cell; cDC, conventional dendritic cell; Mig. cDC, migratory cDC; pDC, plasmacytoid DC; NK cell, natural killer cell; HSC, hepatic stellate cell. (C) Violin plot showing expression levels of marker genes in each cell type. Detailed

timepoints following intrahepatic inoculation with HCV RNA. Animals were divided into acute (1 wpi) and long-term (111 wpi) groups receiving either 10 μg or 30 μg of viral RNA, alongside PBS-injected controls at corresponding timepoints (Fig. 1A). Fresh liver samples were subjected to scRNA-seq in all animals, while snRNA-seq was additionally performed on samples from the acute infection group (Fig. 1A).

In total, 236,610 single-cell or single-nucleus transcriptomes were captured. After rigorous quality control filtering (>200 genes per cell and >3 cells per gene), 157,298 high-quality cells were retained for downstream analysis (Supplementary Fig. S2a–S2c). Dimensionality reduction via UMAP, coupled with unsupervised clustering, identified 16 transcriptionally distinct liver cell clusters (Fig. 1B and Supplementary Table S4). Differential expression analysis (FDR $<1 \times 10^{-5}$) was used to identify differentially expressed genes (DEGs) for each cell cluster (Supplementary Table S4), and cell types were annotated based on well-established markers with clear biological relevance (Fig. 1C and Supplementary Fig. S2e). Among the 16 major cell types identified, parenchymal hepatocytes (n = 49,435) were defined by canonical expression of *HNF4A*, *TAT*, and *CYP2E1*, while cholangiocytes (n = 961) were marked by *MMP7* and *KRT7*. Non-parenchymal cells (NPCs, n = 106,902) comprised both immune and stromal cell populations. Immune cells, identified by *PTPRC* expression, were further subdivided into myeloid and lymphoid lineages. Myeloid subsets included neutrophils (n = 9549; *CSF3R* and *CXCR1*), conventional dendritic cells (cDCs) (n = 7507; *XCR1*), plasmacytoid DCs (pDCs) (n = 7293; *CLEC4C*), monocytes (n = 6156; *FCGR3A*), Kupffer cells (n = 11,829; *VSIG4*, *C1QB*, and *TIMD4*), basophils (n = 382; *CSF2RB*), and erythroblasts (n = 2629; *TFRC*, *GYPA*, and *AHSP*). Lymphoid cell types were represented by T cells (n = 30,066; *LCK*, *GZMK*, and *IL7R*), natural killer cells (NKs) (n = 12,209; *NCR1* and *IL2RB*), B cells (n = 5194; *IGHM* and *CD19*), and plasma cells (n = 4622; *EDEM1* and *JCHAIN*). The remaining clusters encompassed stromal elements, including endothelial cells (n = 8208), hepatic stellate cells (n = 1090), and fibroblasts (n = 168).

In alignment with prior single-cell and single-nucleus transcriptomic atlases of the liver,[58,59] the cellular compositions captured by scRNA-seq and snRNA-seq in tree shrew liver samples differed markedly (Fig. 1D and Supplementary Fig. S2d), indicating methodological biases in cell-type recovery. Notably, hepatocytes were predominantly captured by snRNA-seq, while immune cells were primarily captured by scRNA-seq (Supplementary Fig. S2d). To comprehensively assess cellular responses to HCV, datasets from both platforms were integrated across HCV-inoculated and PBS-treated groups. Comparative analysis revealed shifts in the relative abundance of specific cell types following HCV RNA inoculation (Fig. 1E). For instance, erythroblasts constituted up to 9.5% of liver cells at 1 wpi but were nearly absent in control samples. Neutrophils were also elevated in the inoculated group compared to the corresponding control group at both acute (1 wpi) and long-term (111 wpi) stages (Fig. 1E).

Global transcriptomic profiles revealed pronounced separation between the PBS and JFH1-inoculated groups across major cell types (Fig. 1F and Supplementary Fig. S2c), suggesting widespread transcriptional remodelling in response to viral RNA. Given that non-polyadenylated HCV genomes could not be captured by scRNA-seq or snRNA-seq, interferon (IFN)-stimulated gene (ISG) expression profiles were used to infer the magnitude of antiviral activation. HCV RNA inoculation induced a significant increase in ISG expression relative to PBS-treated controls (Fig. 1G and Supplementary Fig. S2f), indicating activation of the innate immune response by HCV RNA. Although variations in viral RNA dosage (10 μg and 30 μg) at 111 wpi contributed to some degree of transcriptional modulation, these effects were relatively minor compared to the differential responses observed between the control and infected groups (Fig. 1F). Elevated ISG expression was observed across all hepatic cell types in the inoculated samples, with the most pronounced induction detected at 1 wpi (Supplementary Fig. S3a and S3b), highlighting IFN-driven responses as a dominant feature of the early hepatic reaction to HCV RNA exposure.

Zonation of ISGs in hepatocytes during acute HCV challenge

Hepatocytes, comprising the bulk of the liver parenchyma, represent the principal target of HCV infection.[60] At 1 wpi, a total of 49,435 hepatocytes were identified using snRNA-seq (Fig. 2A), enabling a detailed examination of early hepatocellular responses to viral RNA. Analysis of known HCV entry factors, including *CLDN1*, *SCARB1*, *EPHA2*, *TFRC*, and *NPC1L1*, revealed increased expression of *CLDN1*, *TFRC*, and *NPC1L1* in hepatocytes following

information is listed in Supplementary Table S4. (D) Bar plot showing relative proportion of each liver cell type in each sample. Cell types are colour-coded according to UMAP in Fig. 1B. Prefix "sc" in sample ID denotes scRNA-seq and "sn" denotes snRNA-seq. (E) Stacked bar plot showing relative distribution of distinct cell clusters across experimental groups at critical infection timepoints (1 wpi versus 111 wpi). (F) UMAP visualisation of single cells in each group under two different conditions (1 wpi and 111 wpi). (G) UMAP visualisation of interferon-stimulated gene (ISG) score in tree shrew liver cells at 1 wpi and 111 wpi. Colour key from blue to red represents low to high gene expression levels.

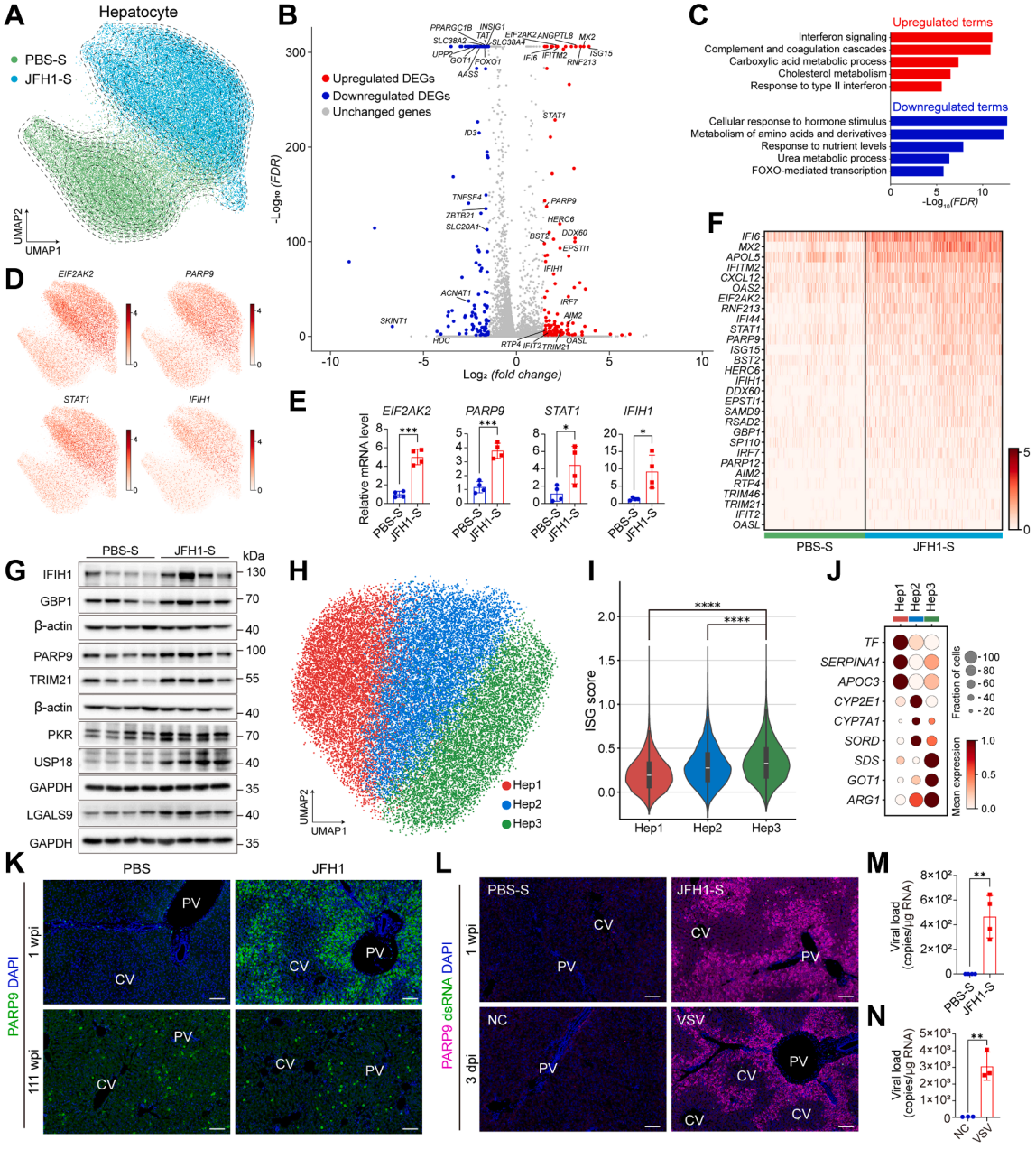

Fig. 2: **Hepatocyte responses and spatial ISG zonation in tree shrew livers following acute HCV inoculation.** (A) UMAP visualisation of hepatocytes coloured by inoculation status (HCV RNA (JFH1-S) versus PBS-S). (B) Volcano plot of DEGs between PBS-S and JFH1-S groups. Upregulated, downregulated, and unchanged genes are indicated by different colours. Detailed information is listed in Supplementary Table S5. (C) Functional enrichment analysis of upregulated (red) and downregulated (blue) DEGs ($|\log_2$ (fold change)$|$ > 1, FDR <1 × 10^{-5}, top 500 genes) between PBS-S and JFH1-S groups. (D) UMAP visualisation of hepatocytes coloured by expression levels of four ISGs. (E) Quantification of mRNA levels of four ISGs in tree shrew liver tissues. mRNA level of each ISG was normalised to *β-actin*. *n* = 4 animals per group. (F) Heatmap showing expression levels of major ISGs in hepatocytes between PBS-S and JFH1-S groups. (G) Protein expression of representative ISGs in tree shrew livers from PBS-S and JFH1-S groups. (H–J) Subcluster characterisation of hepatocytes in JFH1-S group. (H) UMAP visualisation of hepatocytes from JFH1-S group coloured by subclusters. (I) Violin plot of ISG score in three hepatocyte subclusters in (H). (J) Dot plot showing expression levels of representative marker genes in each hepatocyte subcluster. Size of dots is proportional to percentage of cells expressing that gene, with colour scales showing average expression levels. (K) Immunofluorescence images of PARP9 (green) in tree shrew livers at 1 wpi and 111 wpi, with nuclei stained by DAPI (blue). (L) Immunofluorescence images of PARP9 (magenta) and dsRNA (green) in liver tissues from tree shrews with acute HCV RNA inoculation (top, JFH1-S group, 1 wpi),

inoculation (Supplementary Fig. S4a). The expression of CD81, OCLN, and CLDN1 at the protein level was validated by western blotting analysis of liver lysates from inoculated animals (Supplementary Fig. S4b and S4c), with *CLDN1* showing marked elevation in the JFH1-S group compared to the control group (Supplementary Fig. S4c and S4d). These findings suggested that the expression dynamics of CLDN1 might correlate with HCV inoculation in tree shrews.

Dimensional reduction and clustering of hepatocytes at 1 wpi revealed clear separation between the PBS-S and JFH1-S groups (Fig. 2A), indicating substantial transcriptional remodelling in response to early-stage HCV RNA inoculation. Differential gene expression analysis identified various upregulated transcripts in the infected group (Fig. 2B), with enrichment in pathways involved in "interferon signalling", "complement and coagulation cascades", and "carboxylic acid metabolic process" (Fig. 2C). A pronounced upregulation of canonical ISGs, including *IFI6*, *EIF2AK2*, *PARP9*, *STAT1*, *IFIH1*, and *ISG15*, was observed in hepatocytes from the JFH1-S group (Fig. 2D–F). Elevated expression of representative ISGs (*EIF2AK2*, *PARP9*, *STAT1*, and *IFIH1*) was further validated by qRT-PCR (Fig. 2E) and western blotting (Fig. 2G and Supplementary Fig. S4e) in liver tissues from the JFH1-S group compared to the PBS-S group. These results suggest that HCV inoculation triggers robust IFN signalling and activates a broad antiviral program in hepatocytes.

To further dissect hepatocellular heterogeneity in response to HCV RNA, single-nucleus transcriptomes from liver samples at 1 wpi were analyzed, revealing three distinct hepatocyte subclusters (Hep1, Hep2, and Hep3; Fig. 2H), each defined by unique transcriptional signatures. Among the three subclusters, Hep3 exhibited the highest ISG score, followed by Hep2 (Fig. 2I). Spatial marker analysis indicated that Hep2 was enriched in genes typically expressed in the pericentral vein (CV), including *CYP2E1*, *CYP7A1*, and *SORD*, whereas Hep3 showed elevated expression of *SDS*, *GOT1*, and *ARG1* in the periportal vein (PV) (Fig. 2J). These results suggest that activated ISGs are preferentially activated in periportal hepatocytes. Immunofluorescence staining further validated these observations, showing periportal upregulation of representative ISGs, such as PARP9 and STING, in liver sections from HCV-inoculated animals at 1 wpi (Fig. 2K and Supplementary Fig. S4f). In contrast, at 111 wpi, PARP9 expression was dispersed across the hepatic lobule, without clear periportal localisation (Fig. 2K). These spatial dynamics imply that initial restriction of HCV RNA may be localised to periportal hepatocytes. Despite clear evidence of ISG activation, immunofluorescence failed to detect double-stranded HCV RNA (dsRNA), the replicative intermediate typically required to activate IFN signalling, in liver tissues at 1 wpi (Fig. 2L), although a relatively low HCV viral load was detected in the same samples (Fig. 2M). This result suggested that the zonal distributions of ISGs help with rapid viral clearance in hepatocytes. In addition to ISG zonation, periportal enrichment of *CLDN1*, a critical HCV entry factor, was also observed at 1 wpi (Supplementary Fig. S4g and S4h). As intrahepatic injection of HCV RNA was a lack of receptor-mediated infection, we speculated that *CLDN1* upregulation at 1 wpi was induced by host sensing of HCV RNA. The exact role of the CLDN1 upregulation (direct HCV RNA sensing, receptor of HCV entry, or as a potential ISG) upon HCV RNA inoculation and its underlying mechanism remained to be investigated.

To further investigate whether ISG zonation was associated with stimulations by different viruses or different routes of viral inoculation, tree shrews were intravenously injected with VSV-GFP and AAV8-mCherry viruses, with liver tissues, and then examined for restricted expression of ISGs in periportal hepatocytes. At 3 days post-injection (3 dpi) with VSV-GFP, robust expression of PARP9 was observed specifically in periportal hepatocytes (Fig. 2L), mirroring the pattern detected following HCV RNA inoculation. Despite the presence of measurable VSV RNA, as confirmed by qRT-PCR, immunofluorescence assays failed to detect VSV dsRNA(Fig. 2L, N). In contrast, liver tissues from tree shrews infected with AAV8-mCherry at 4 wpi exhibited no evidence of periportal-restricted PARP9 expression. Instead, expression was dispersed, with enrichment in pericentral zone (Supplementary Fig. S4i). This distribution was consistent regardless of whether the AAV8 vector carried the hepatocyte-specific TBG promoter or the broadly active CAG promoter. Therefore, the zonal distributions of ISGs in response to HCV RNA (intrahepatic injection) or VSV-GFP (intravenous injection) and pericentral expression of AAV8-mCherry (intravenous injection) were unlikely caused by different inoculation routes that involved different patterns of liver blood flow (portal for intrahepatic injection versus

intravenous injection of VSV-GFP (bottom, 3 dpi, 3 days post-infection), and related controls (PBS-S and NC). Nuclei were stained with DAPI (blue). Animals were sacrificed for liver tissue collection on 3 dpi of VSV-GFP. NC, negative control, injected with culture medium. (M) HCV RNA levels in liver tissues of JFH1-S group relative to PBS-S group. $n = 4$ animals per group. (N) VSV RNA levels in liver tissues from tree shrews intravenously injected with VSV-GFP (VSV) or culture medium (NC). $n = 3$ animals per group. Scale bars in (K–L), 100 μm. PV, portal vein; CV, central vein. The Kruskal-Wallis test followed by Dunnett's multiple comparisons test for (I). Two-tailed unpaired Student's *t*-test for (E, M, and N). Data in (E, M, and N) are presented as mean ± SD. *, $P < 0.05$; **, $P < 0.01$; ***, $P < 0.001$; ****, $P < 0.0001$.

systemic for intravenous injection). These findings suggested that innate immune restriction may be spatially zonated during the early antiviral response, confining HCV RNA and VSV-GFP to the periportal region. However, once productive infection is established, as exemplified by AAV8-mCherry, viral dissemination appears to extend toward the pericentral zone, potentially overriding localised immune defenses in the periportal zone. Taken together, these results indicated that HCV RNA in tree shrews might be restricted and cleared by activated immune response and ISG zonation in periportal hepatocytes.

To explore the molecular underpinnings of hepatocyte zonation in the context of HCV RNA exposure, DEGs from Hep2 to Hep3 subclusters at 1 wpi were cross-referenced with zone-specific gene signatures derived from mouse liver.[28] Of the 248 overlapping spatially defined genes, 56 were enriched in Hep2 and 192 were enriched in Hep3. Comparative analysis between JFH1-S and PBS-S groups revealed significant alterations in 111 of these genes, including 37 upregulated (16 CV and 21 PV) and 74 downregulated (12 CV and 62 PV genes) transcripts (Supplementary Fig. S4j, k). In particular, 16 of these altered genes, including CV genes (*ARRDC3*, *CSAD*, and *KLF9*) and PV genes (*SMIM27*, *THRSP*, *MID1IP1*, *COQ10B*, *CPS1*, *PPARGC1A*, *G6PC*, *SORBS2*, *SLC25A25*, *PCK1*, *AASS*, *NNMT*, and *TAT*), were also significantly altered in bulk RNA isolated from whole liver tissues of the JFH1-S group. Functional enrichment analysis revealed that many of these Hep2- and Hep3-specific genes were enriched in key metabolic processes (Supplementary Fig. S4l and S4m), suggesting that HCV-induced transcriptional reprogramming includes spatially organised metabolic remodelling. This shift in hepatocellular metabolism may reduce the availability of critical substances required for efficient viral replication and concurrently modulate the host immune response.[61,62]

HCV infection disrupts glucose metabolism in tree shrews

Transcriptomic profiling of hepatocytes at 1 wpi revealed that HCV RNA inoculation induced widespread transcriptional repression of genes associated with core hepatic metabolic functions. Enrichment analysis of downregulated genes identified significant suppression of pathways related to amino acid metabolism, urea cycle, glycolysis, and gluconeogenesis (Figs. 2C and 3A). The urea cycle, a critical metabolic pathway, occurs exclusively in the liver.[63] Key urea cycle genes, including *CPS1*, *ASS1*, *ASL*, *ARG1*, and *SLC25A15*, were markedly downregulated in hepatocytes (Fig. 3A), suggesting functional impairment of ammonia clearance following HCV RNA inoculation. These findings align with previous reports implicating type I IFN signalling in the transcriptional repression of urea cycle genes during viral infection.[64] Amino acid metabolism was similarly affected. Several key enzymes were suppressed in hepatocytes, including tyrosine aminotransferase (*TAT*), the rate-limiting enzyme of the tyrosine degradation pathway, glutamic oxaloacetic transaminase 1 (*GOT1*), involved in glutamine metabolism and redox balance, and alanine-glyoxylate aminotransferase (*AGXT*), which regulates glyoxylate detoxification through transamination (Fig. 3A). However, the mechanism by which HCV RNA perturbs these pathways in hepatocytes remains unclear.

Suppression of glucose metabolism was another prominent finding, given its crucial role in cellular activities.[66] Notably, hepatocyte expression of genes involved in gluconeogenesis, including *FOXO1*, *PCK1*, *G6PC*, *PPARGC1A*, and *IGFBP1*, was significantly decreased following HCV RNA inoculation (Fig. 3A). These transcriptomic changes were confirmed at the mRNA and protein levels in liver tissues collected at 1 wpi (Fig. 3B, C and Supplementary Fig. S5a). Consistent with these findings, tree shrews from the JFH1-S group exhibited significantly reduced blood glucose levels compared to the PBS-S group (Fig. 3D). Similarly, phosphorylation of AMPK at Thr172, a key sensor of cellular glucose,[67] was significantly elevated in the livers of HCV-inoculated tree shrews at 1 wpi (Fig. 3C and Supplementary Fig. S5a), indicating the active involvement of glucose metabolism in hepatocytes following HCV RNA inoculation.

To validate the glycometabolic reprogramming observed in HCV-inoculated tree shrew livers, the tree shrew hepatic cell line ITH6[50] was infected with HCV and compared to Huh7 (a highly permissive human hepatoma cell line) and reported PHHs data.[65] Similar to the reduced level of serum glucose observed in HCV-inoculated tree shrews (Fig. 3D), ITH6 cells exhibited significant time-dependent glucose depletion in the culture medium at 24, 48, and 72 h post-infection (hpi), accompanied by increasing the inoculum dosage. In contrast, glucose concentrations remained unchanged in HCV-infected Huh7 cells over the same period (Fig. 3E). Correspondingly, HCV-infected ITH6 cells demonstrated significantly elevated lactate production at 48 hpi, indicative of a shift towards glycolytic metabolism. This response was absent in Huh7 cells (Fig. 3F). Transcriptomic profiling at 48 and 72 hpi revealed strong upregulation of ISGs and pro-inflammatory factors in ITH6 cells upon HCV infection (Fig. 3G), recapitulating the transcriptional landscape observed in infected tree shrew livers at 1 wpi (Fig. 2B, C). Notably, glycolytic regulators such as *HK2*, *PGK1*, and *SLC2A1* were significantly induced in ITH6 cells and in primary tree shrew hepatocytes (PTHs), as confirmed using qRT-PCR (Fig. 3H). These immune and metabolic signatures were also observed in HCV-infected PHHs but not in HCV-infected Huh7 cells (Fig. 3G), likely due to the defective IFN response in Huh7 cells,[68] which failed to trigger the immune-

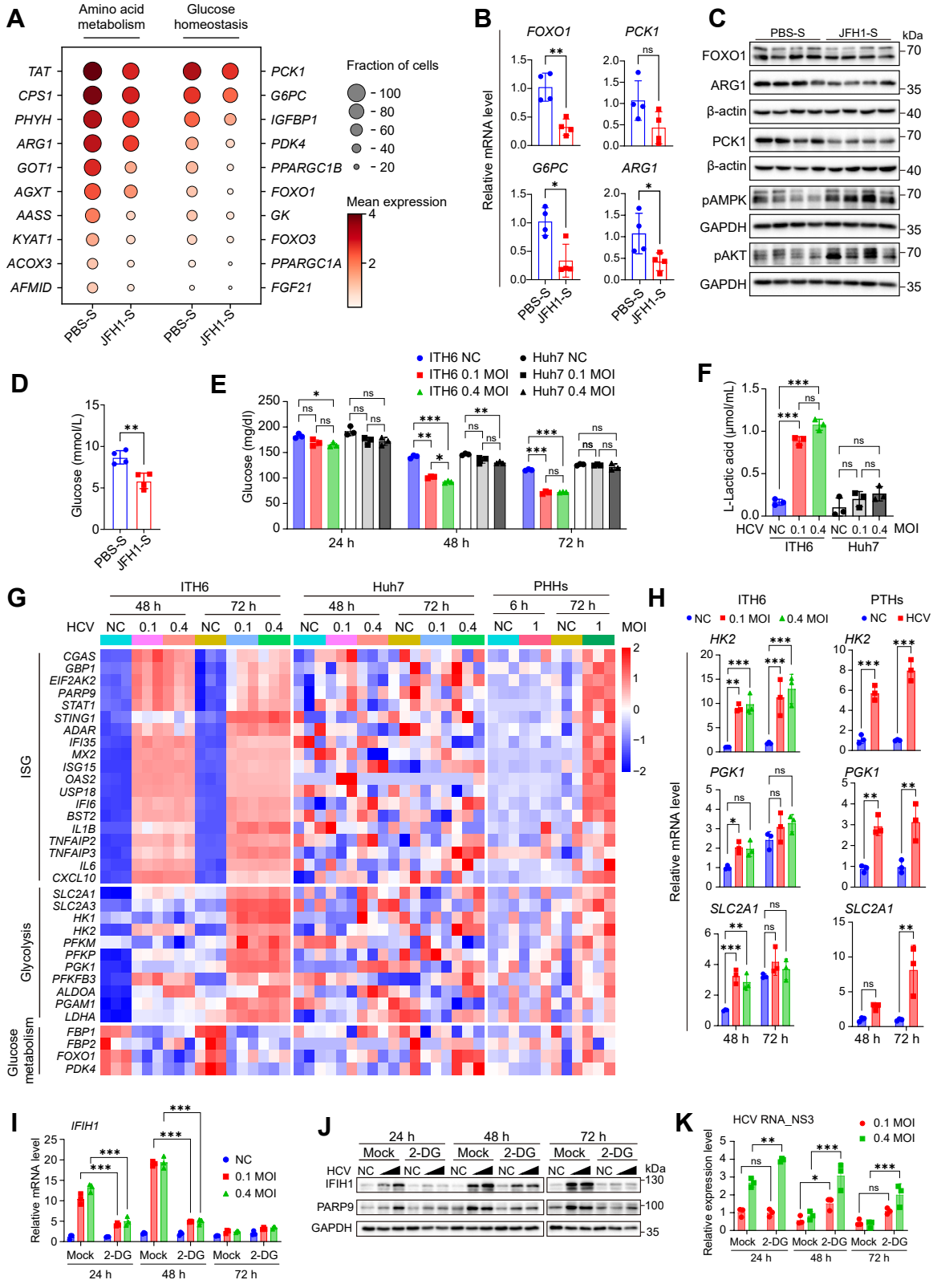
A
Amino acid metabolism
Glucose homeostasis
TAT
CPS1
PHYH
ARG1
GOT1
AGXT
AASS
KYAT1
ACOX3
AFMID
PCK1
G6PC
IGFBP1
PDK4
PPARGC1B
FOXO1
GK
FOXO3
PPARGC1A
FGF21
PBS-S
JFH1-S
Fraction of cells
Mean expression
B
FOXO1
PCK1
G6PC
ARG1
Relative mRNA level
C
PBS-S
JFH1-S
kDa
FOXO1
ARG1
β-actin
PCK1
pAMPK
GAPDH
pAKT
D
Glucose (mmol/L)
E
ITH6 NC
ITH6 0.1 MOI
ITH6 0.4 MOI
Huh7 NC
Huh7 0.1 MOI
Huh7 0.4 MOI
Glucose (mg/dl)
24 h
48 h
72 h
F
L-Lactic acid (μmol/mL)
HCV
MOI
ITH6
Huh7
G
ITH6
Huh7
PHHs
48 h
72 h
6 h
HCV
NC
0.1
0.4
1
MOI
ISG
CGAS
GBP1
EIF2AK2
PARP9
STAT1
STING1
ADAR
IFI35
MX2
ISG15
OAS2
USP18
IFI6
BST2
IL1B
TNFAIP2
TNFAIP3
IL6
CXCL10
Glycolysis
SLC2A1
SLC2A3
HK1
HK2
PFKM
PFKP
PGK1
PFKFB3
ALDOA
PGAM1
LDHA
Glucose metabolism
FBP1
FBP2
FOXO1
PDK4
H
ITH6
PTHs
NC
0.1 MOI
0.4 MOI
HCV
HK2
PGK1
SLC2A1
Relative mRNA level
48 h
72 h
I
IFIH1
Relative mRNA level
NC
0.1 MOI
0.4 MOI
Mock
2-DG
24 h
48 h
72 h
J
24 h
48 h
72 h
Mock
2-DG
HCV
IFIH1
PARP9
GAPDH
kDa
K
HCV RNA_NS3
0.1 MOI
0.4 MOI
Relative expression level
Mock
2-DG
24 h
48 h
72 h

metabolic crosstalk. The contrasting permissiveness to HCV between Huh7 and ITH6 cells fundamentally shaped their distinct transcriptomic responses, (partially) accounting for the divergent patterns of virus-host interactions observed in each system (Fig. 3G).

To delineate the role of glucose metabolism in regulating antiviral responses during HCV infection, the impact of glycolytic inhibition on interferon signalling and viral replication was examined in ITH6 cells. Cells were treated with or without 2-deoxy-D-glucose (2-DG), a competitive inhibitor of glycolysis, and assessed for expression of key ISGs at 24, 48, and 72 hpi. Compared to untreated controls, 2-DG treatment led to a marked suppression of ISG transcripts, including *IFIH1*, *PARP9*, and *MX1* at 24 and 48 hpi (Fig. 3I, J and Supplementary Fig. S5b). This attenuation of the innate immune response was accompanied by a significant increase in intracellular HCV RNA levels, despite a gradual decline in viral RNA over time (Fig. 3K and Supplementary Fig. S5c). Note that HCV core and NS3 proteins remained undetectable by western blotting (data not shown). To further confirm the metabolic dependence of ISG expression, ITH6 cells were treated with R-GEN-140, a selective inhibitor of lactate dehydrogenase A (LDHA). Similar to 2-DG, R-GEN-140 suppressed *IFIH1* and *PARP9* expression while promoting accumulation of intracellular HCV RNA (Supplementary Fig. S5d and S5e), reinforcing the notion that glycolytic flux supports antiviral transcriptional responses in tree shrew hepatic cells. Together, these findings demonstrated that inhibition of glycolysis dampens innate immune activation and facilitates viral accumulation in ITH6 cells.

To determine whether this regulatory mechanism extends to human hepatic cells, parallel experiments were conducted in Huh7 cells. Unlike ITH6, HCV infection did not significantly affect the mRNA expression of glucose metabolism-related genes in Huh7 cells (Fig. 3G). Nonetheless, inhibition of glycolysis with 2-DG reduced HCV NS3 and core protein level at 48 hpi under glucose-rich conditions, although this reduction was not apparent at 72 hpi. Switching the culture medium from glucose to galactose resulted in a substantial reduction in viral protein expression, with 2-DG exerting a more pronounced inhibitory effect under these conditions (Supplementary Fig. S5f). In galactose-containing medium, 2-DG completely attenuated detectable levels of HCV NS3 and core proteins (Supplementary Fig. S5f). Collectively, the inhibition of glycolysis and conversion of carbohydrate sources affected HCV production in Huh7 cells. In contrast, tree shrew hepatocytes appear to utilise glycolysis to enhance antiviral innate immunity and restrict the replication of HCV, potentially explaining intermittent viraemia observed during HCV infection in tree shrews. It will be worthwhile to investigate whether HCV similarly utilises glycolysis and subverts the innate immune response to establish infection in PHHs.

Increase in erythroblasts in tree shrew livers upon HCV inoculation

Single-cell transcriptomic analysis revealed a striking enrichment of erythroblasts in the liver of tree shrews at 1 wpi, with a total of 2507 erythroblast cells identified. In contrast, only 36 erythroblasts were detected in the PBS-treated controls (Fig. 4A). These cells were defined as nucleated immature erythroid precursors based on co-expression of canonical surface markers CD235a (glycophorin A, *GYPA*) and CD71 (transferrin receptor, *TFRC*).[69] Additional erythroid lineage-specific markers, including *AHSP*, *GATA1*, *HEMGN*, *ALAS2*,

***Fig. 3:* HCV infection disrupts glucose metabolism and modulates innate immune responses in tree shrew livers and cultured hepatic cells.** (A) Dot plot showing expression of genes involved in amino acid and glucose homeostasis in tree shrew livers at 1 wpi. Size of dots is proportional to percentage of cells expressing that gene, and colour scale shows average expression level. (B) mRNA levels of genes *FOXO1*, *PCK1*, *G6PC* and *ARG1* in liver tissues between PBS-S and JFH1-S groups. Gene expression was detected by qRT-PCR, normalised to *β-actin*. (C) Protein levels of FOXO1, ARG1, PCK1, pAMPK, and pAKT in liver tissues between PBS-S and JFH1-S groups. (D) Serum glucose levels in tree shrews between PBS-S and JFH1-S groups. (E) Glucose levels in culture medium of HCV-infected and mock-infected (NC) ITH6 and Huh7 cells. ITH6 and Huh7 cells were infected with HCV at two multiplicities of infection (MOIs) of 0.1 or 0.4 for 24, 48, and 72 h, respectively. (F) Lactic acid levels in culture medium of ITH6 and Huh7 cells with HCV infection or mock infection (NC). Culture medium was collected at 48 h after infection. (G) Heatmap showing the expression level of ISGs, glycolytic, and glucose metabolism-related genes (using Z-score for normalised TPM value) in ITH6, Huh7 cells and primary human hepatocytes (PHHs) infected with or without HCV at different MOIs. Colour key from blue to red represents low to high gene expression levels. Original dataset for PHHs (GSE132548) was reported by Vieyres et al.[65] (H) Validation for mRNA levels of three glycolysis genes in ITH6 cells and primary tree shrew hepatocytes (PTHs) with or without HCV infection (MOI = 1). Cells were harvested at 48 h and 72 h after HCV infection. (I) mRNA expression level of *IFIH1* in ITH6 cells with or without 2-DG treatment. ITH6 cells were first infected with or without HCV (MOI = 0.1 or 0.4) for 6 h, then switched to culture medium supplemented with 2-DG (2 mM). Cells were harvested at 24, 48, and 72 hpi for qRT-PCR. (J) Protein expression level of IFIH1 and PARP9 in ITH6 cells. Cells received the same treatment as in (I). (K) Quantification of intracellular HCV RNAs in ITH6 Cells. Cells received the same treatment as in (I). HCV genomic NS3 gene was detected by qRT-PCR. Data are presented as mean ± SD. Two-tailed unpaired Student's *t*-test was used for (B, D, $n = 4$ animals per group). Two-way repeated measures ANOVA with the Geisser-Greenhouse correction, Tukey's multiple comparisons test was used for (E). One-way ANOVA with Tukey's multiple comparisons test was used for (F). Two-way ANOVA with Tukey's multiple comparisons test was used for (H, I, K). $n = 3$ biological replicates at each time point (24 h, 48 h and/or 72 h) in (E, F, H-I, K). ns, not significant; *, $P < 0.05$; **, $P < 0.01$; ***, $P < 0.001$.

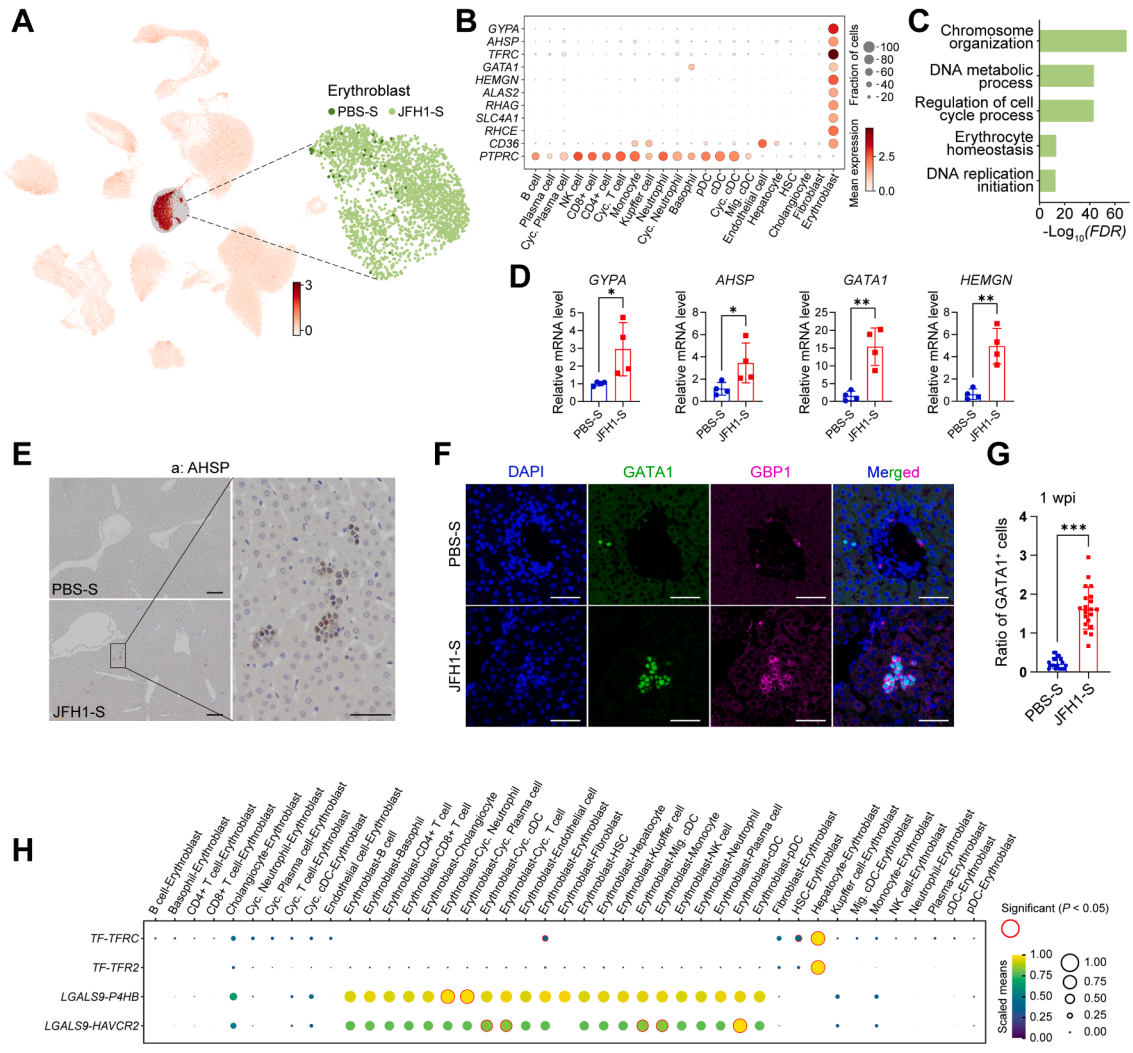

Fig. 4: **Enrichment of erythroblasts in liver tissues of tree shrews following acute HCV inoculation.** (A) UMAP visualisation of erythroblasts (dark red) in liver tissues of tree shrews at 1 wpi, with enlarged view showing erythroblasts from PBS-S and JFH1-S groups. (B) Dot plot showing expression levels of marker genes in erythroblasts and other cell types from tree shrew livers. Size of dots represents percentage of cells expressing the indicated marker gene, with colour key from grey to red showing low to high gene expression. (C) Bar chart showing functional enrichment analysis in erythroblasts based on DEGs (log_2 (fold change) > 0.5, FDR <1 × 10^{-5}, top 500 genes). (D) mRNA level of representative erythroid lineage genes in tree shrew livers of PBS-S and JFH1-S groups. *n* = 4 animals per group. (E) Representative immunohistochemical staining of AHSP in liver tissues from PBS-S and JFH1-S groups. Scale bar, 200 μm for liver section (*left*) and 50 μm for enlarged view of boxed areas (*right*). (F) Representative immunofluorescence images of GATA1 (*green*) and GBP1 (*magenta*) in liver tissues from PBS-S and JFH1-S groups. Scale bar, 50 μm. (G) Percentage of GATA1-positive cells in total number of liver cells based on (F). Data were obtained from five independent fields of view per tissue slice. For each animal, one tissue slice was analyzed. *n* = 4 animals per group. (H) Dot plot showing significant ligand-receptor pairs involved in interactions between erythroblasts and all other cell types. Red circle represents interaction with significant difference ($P < 0.05$). Average means of potential interactions between ligands and receptors are indicated by colour and circle size. Two-tailed unpaired Student's *t*-test for (D) and the Mann-Whitney test for (G). Data in (D and G) are presented as mean ± SD. ns, not significant; *, $P < 0.05$; **, $P < 0.01$; ***, $P < 0.001$.

RHAG, *SLC4A1*, and *RHCE*, were overexpressed in erythroblasts during the acute stage of HCV infection (Fig. 4B). Functional enrichment analysis of DEGs in erythroblasts revealed strong associations with pathways regulating chromosome organisation, DNA metabolism, and cell cycle progression (Fig. 4C). These transcriptomic patterns were validated by qRT-PCR in liver tissues (Fig. 4D) and further confirmed by immunohistochemical (Fig. 4E) and immunofluorescence analyses (Fig. 4F, G). Intriguingly, erythroblasts

expressing GATA1, a haematopoietic transcription factor, also exhibited upregulated expression of GBP1, a typical ISG (Fig. 4F), in liver tissues of HCV-inoculated tree shrews. In addition, we observed only a very small number of erythroblasts in liver tissue sections from the tree shrews infected with VSV-GFP, AAV8-mCherry virus and treated with IFNα (Supplementary Fig. S6a).

During embryogenesis, erythropoiesis transitions from the yolk sac to the foetal liver before migrating to the bone marrow in the postnatal period.[70,71] Analysis of foetal liver gene expression in tree shrews revealed that key erythroid genes were highly expressed from embryonic day 26 (E26) to E37, with progressive downregulation by postnatal day 3 and a marked decline by day 8 (Supplementary Fig. S6b), consistent with the developmental migration of haematopoiesis from liver to bone marrow. This temporal pattern explains the near-complete absence of erythroblasts in healthy young tree shrew livers and supports the notion that their reappearance at 1 wpi reflects a liver-specific haematopoietic response to HCV RNA inoculation. To assess whether this erythroid response was evolutionarily conserved, erythroblasts identified in tree shrew livers were compared with those present in steady-state mouse livers.[45] Cross-species analysis revealed highly similar lineage distributions (Supplementary Fig. S6c), with conserved expression of key erythroid regulators, including *TFRC*, *GATA1*, and *HEMGN* (Supplementary Fig. S6d).

Erythroid-lineage cells, traditionally regarded for their role in oxygen transport, have increasingly been recognised for their immunomodulatory functions.[72] To explore the potential impact of erythroblasts on other cell types during HCV inoculation in tree shrew livers, CellphoneDB[44] was employed to analyse intercellular communication networks and ligand-receptor interactions among cell populations. Results revealed a wide array of ligand-receptor interactions between erythroblasts and multiple hepatic cell populations (Fig. 4H). Among the identified interactions, transferrin (TF)-transferrin receptor (TFRC) binding and TF-transferrin receptor 2 (TFR2) binding between hepatocytes and erythroblasts likely reflect a coordinated regulation of iron uptake critical for erythroblast development. Beyond iron metabolism, erythroblasts also engaged in immunomodulatory signalling. Notably, LGALS9 (Gal-9)-P4HB interactions were observed between erythroblasts and cycling neutrophils and plasma cells (Fig. 4H), implicating this axis in the modulation of cell migration and T-cell inhibition.[73] Additionally, LGALS9 (Gal-9)-HAVCR2 (TIM-3) interactions were observed between erythroblasts and immune cells, including T cells, cDCs, and monocytes. Gal-9 is known to be inducible by several viruses, including HCV,[74] and its engagement of TIM-3 functioned as an inhibitory molecule within the immune checkpoints. Gal-9-TIM-3 interactions have been shown to induce apoptosis of T cells in cancer models.[75] Collectively, these ligand-receptor networks suggest that erythroblasts in the HCV-inoculated tree shrew liver may exert immunoregulatory effects, potentially suppressing overactive immune responses through targeted suppression of T-cell and myeloid cell activity.

Neutrophil subsets exhibit distinct functional states in response to HCV RNA inoculation

Neutrophils are frontline effectors of innate immunity, rapidly mobilised to sites of tissue injury or infection to initiate host defence.[76] In tree shrews, HCV RNA inoculation led to a marked expansion of hepatic neutrophil populations (Fig. 1E), prompting detailed analysis of their heterogeneity and functional states. Single-cell transcriptomic profiling identified 5469 neutrophils at 1 wpi and 4080 neutrophils at 111 wpi (Fig. 5A). Unsupervised clustering resolved three transcriptionally distinct neutrophil subpopulations—Neu1, Neu2, and Neu3—each comprising cells from both timepoints (Fig. 5A). These clusters exhibited distinct gene expression profiles characterised by the upregulation of a subset of genes, suggesting functional specialisation within the neutrophil compartment (Fig. 5B and Supplementary Fig. S7a). Neu1, the most abundant subcluster, displayed upregulation of ISGs (Fig. 5C) and elevated expression of chemotaxis- (*CXCR1*, *CSF3R*, and *LGALS3*) and inflammatory response-related genes (*ALOX5AP*, *TYROBP*, *FTH1*, *C5AR1*, and *IL1B*) (Fig. 5B). Neu2 exhibited a transcriptional signature indicative of proliferative activity, marked by cell cycle-associated genes (*MKI67*, *TOP2A*, *STMN1*, and *CDK1*), antibacterial effectors (*CAMP*), and structural maintenance of chromosome (SMC) genes (*SMC2*, *SMC4*). In contrast, Neu3 displayed strong expression of azurophilic granule genes, such as *ELANE* (encoding neutrophil elastase (NE)), *CTSG*, and *SLPI* (Fig. 5B). Trajectory analysis revealed three distinct activation states across the neutrophil landscape, with downregulation of *ALOX5AP*, *MS4A4A*, and *CCL15* at the quiescent C1 state, upregulation of cell-cycle regulators (*MKI67* and *TOP2A*) and protease activation (*CTSG* and *ELANE*) at the proliferative C2 state, and intermediate expression of matrix remodelling (*MMP9*) and antimicrobial effectors (*S100A8*, S100A9, *S100A10*, *CAMP*, and *LYZ*) (Supplementary Fig. S7b). Tracking gene expression changes across these three neutrophil states revealed previously uncharacterised heterogeneity in neutrophil response dynamics during long-term HCV RNA challenge.

Quantitative analysis confirmed that neutrophil abundance significantly increased following HCV RNA inoculation, with the most pronounced expansion observed at 1 wpi (Fig. 5D). Moreover, neutrophil numbers were positively correlated with the inoculum dosage at 111 wpi (Fig. 5E). Consistently, infiltrating

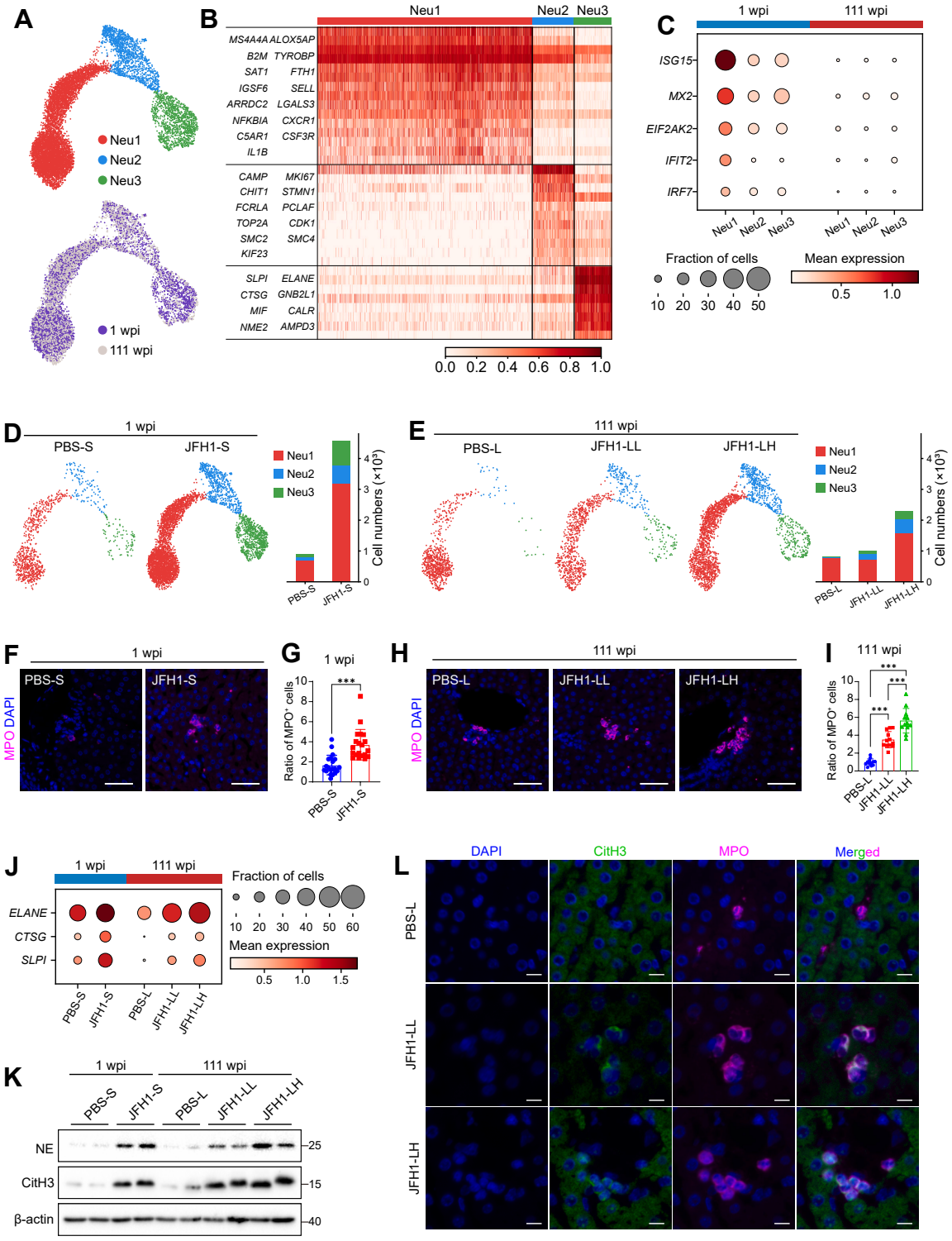

***Fig. 5:* Neutrophils in tree shrew livers following HCV RNA inoculation.** (A) UMAP visualization of neutrophils in livers from tree shrews following acute (1 wpi) and long-term (111 wpi) HCV RNA inoculation. Cells are marked by subclusters (*upper*) and groups (*lower*). (B) Heatmap showing marker genes in three neutrophil subclusters. Color key from gray to red represents low to high gene expression levels. Detailed information is listed in Supplementary Table S6. (C) Dot plot showing expression level of representative ISGs in each neutrophil subcluster. Size of dots is proportional to percentage of cells expressing that gene, with color key from gray to red showing low to high gene

neutrophils also exhibited elevated expression of myeloperoxidase (MPO), representing the accumulation and activation of neutrophils within hepatic tissue (Fig. 5F–I). Beyond phagocytosis, neutrophils also produce cytokines that inhibit viral replication and release neutrophil extracellular traps (NETs) to capture and eliminate viruses.[77] NETs are composed of decondensed DNA, formed in conjunction with citrullinated histone H3 (CitH3), neutrophil elastase (NE), cathepsin G (CTSG), and MPO.[78] NET formation was confirmed by increased expression of NE and CitH3 in liver sections from the JFH1 group compared to the PBS group at both 1 wpi and 111 wpi (Fig. 5J and K, Supplementary Fig. S7c and S7d). In line with this observation, enhanced NET formation was further validated by double-positive cells for CitH3 and MPO in the liver of tree shrews at 111 wpi (Fig. 5L). This finding suggested that despite viral clearance, HCV inoculation induced sustained pathological alterations in the liver even at 111 wpi. These findings indicated that neutrophil populations respond to HCV RNA through distinct and coordinated functional programs—including activation, proliferation, degranulation, and NETs formation—and that their differentiation trajectories are dynamically influenced by viral exposure.

Discussion

Tree shrews have emerged as a promising small mammalian model for HCV infection due to their phylogenetic proximity to primates and the presence of functionally conserved HCV entry factors.[14–19] However, in-depth *in vivo* characterisation of their immune responses to infection has remained limited. In this study, single-cell and single-nucleus transcriptomic profiling, complemented by targeted experimental validation, was used to dissect hepatic immune responses in tree shrews subjected to acute (1 wpi) and long-term (111 wpi) HCV RNA inoculation. This analysis revealed robust and cell type-specific antiviral responses, particularly in hepatocytes, erythroblasts, and neutrophils, providing critical insights into the dynamics of host-virus interactions in this model and highlighting possible explanations for the difficulty in establishing chronic HCV infection model in tree shrews.

Unlike mice, tree shrews exhibit a partial susceptibility to HCV infection, likely due to their conservation of homologous genes encoding key HCV entry factors with high sequence and functional similarity to those of humans. This has been supported by comparative genomics[36] and functional studies of the MAVS signalling axis in tree shrews.[22] Despite this permissiveness, establishing a stable, persistent HCV infection in tree shrews remains challenging. In our study, inoculated animals exhibited intermittent viraemia and persistently low serum viral loads (Supplementary Fig. S1a). Moreover, neither HCV core protein (data not shown) nor replicative dsRNA intermediates were detectable in liver tissues by immunofluorescence, suggesting that viral protein expression may occur at extremely low abundance in this species. This is consistent with observations in chronically HCV-infected human patients, where only a small percentage of hepatocytes express detectable levels of viral proteins despite measurable systemic viraemia.[79–81] These findings underscore the need for more sensitive and quantitative detection methods to assess intrahepatic viral protein expression in future investigations.

The innate immune recognition of HCV RNA is classically mediated by pathogen recognition receptors, including retinoic acid inducible gene-I (RIG-I)-like receptors (RIG-I, MDA5, and LGP2) and TLR3.[82,83] RIG-I is known to bind to the 5′ triphosphate and 3′ poly U/UC motifs of the HCV genome, while MDA5 detects HCV dsRNA replication intermediates.[84,85] LGP2 positively regulates MDA5-mediated signalling, enhancing antiviral responses.[86] The *in vitro*-transcribed HCV RNA used in this study, bearing 5′ triphosphate, can be detected by RIG-I. However, the tree shrew genome lacks RIG-I,[36] which likely alters its innate recognition of RNA viruses. Although MDA5 and LGP2 may partially compensate for this deficiency,[32] the absence of RIG-I likely modulates the amplitude and character of IFN responses in this model. It is plausible that MDA5 mediates recognition of 5′ triphosphate-containing *in vitro*-transcribed HCV RNA, subsequently inducing IFN production and downstream activation of ISGs via

expression levels. (D–E) UMAP visualization of each neutrophil subcluster colored by two groups at 1 wpi (D) and at 111 wpi (E). Stacked bar plot in (D–E) indicates number of neutrophils in each subcluster. (F–G) Representative immunofluorescence images of MPO (*magenta*, neutrophils) in liver tissues from PBS-S and JFH1-S groups (F) and quantification of the ratio of MPO-positive cells (G). Scale bar, 50 μm. Ratio of MPO-positive cells in total number of cells was quantified by counting five independent views in each slice. For each animal, one tissue slice was analyzed. $n = 4$ animals per group. (H–I) Representative immunofluorescence images of MPO (*magenta*) in liver tissues from PBS-L, JFH1-LL, and JFH1-LH groups (H) and quantification of the ratio of MPO-positive cells (I). Scale bar, 50 μm. (J) Dot plot showing expression levels of indicated genes in neutrophils of tree shrew livers at 1 wpi and 111 wpi. Size of dots is proportional to percentage of cells expressing that gene, and color scale shows average expression level. (K) Protein levels of NE and CitH3 in liver tissues from tree shrews with and without HCV RNA inoculation at 1 wpi and 111 wpi. (L) Representative immunofluorescence images of CitH3 (*green*) and MPO (*magenta*) in liver tissues from tree shrews with and without HCV RNA inoculation at 111 wpi. Scale bar, 10 μm. The Mann–Whitney test was used for (G) and one-way ANOVA with Tukey's multiple comparisons test was used for (I). Data in (G and I) are presented as mean ± SD. ***, $P < 0.001$.

receptor engagement in hepatocytes and other immune cells. Consistent with this hypothesis, our results showed that ISG expression was strongly induced across nearly all hepatic cell types following HCV RNA exposure (Supplementary Fig. S3a). Several of these ISGs, such as OASL, DDX60, GBP1, EIF2AK2 (PKR), USP18, ISG15, and STAT1, have previously been implicated in direct antiviral defence, modulation of immune responses, or promotion of viral persistence and treatment resistance[87] (Fig. 2F). However, distinguishing infected from noninfected hepatocytes at single-cell resolution was not feasible in our study, as the transcriptomic platforms employed were incapable of capturing non-poly(A) reads of HCV RNA in hepatic cells. This technical limitation precluded direct mapping of viral replication to host transcriptional phenotypes within hepatocyte subclusters.

Although HCV deploys various immune evasion strategies,[82,88] persistent expression of ISGs has been documented in chronically infected patients,[80] experimentally infected chimpanzees,[89,90] and primary human hepatocytes *in vitro*.[91] The persistence of ISG induction, even in the presence of ongoing viral replication, raises an important question about the mechanisms underlying viral persistence. Rather than eliminating the virus, ISG activation in hepatocytes and immune cells may contribute to hepatic inflammation and immunopathology.[26] In tree shrews, however, HCV appears less capable of evading antiviral responses, likely reflecting distinct genetic and immunological attributes of this species. Our previous study demonstrated that while the viral NS3/4A protease cleaves tree shrew MAVS, it fails to prevent NF-κB activation in primary hepatocytes, thereby maintaining downstream signalling and limiting viral replication.[22] These findings suggested that innate immune pathways remain at least partially intact in tree shrew liver following HCV exposure. Further investigation into species-specific antiviral factors is needed[92] to better understand host restriction mechanisms and their implications for viral clearance.

The identification of spatially enriched ISG expression in hepatocytes from the JFH1 group at 1 wpi, especially within the periportal region, suggests that antiviral innate immune responses may be spatially compartmentalised within the liver. This observation aligns with the established concept of hepatocellular zonation along the portal-central axis, which underpins the metabolic and functional heterogeneity required for hepatic homeostasis.[93] The exact anatomical distribution of HCV-infected hepatocytes in human liver remains unresolved, largely due to the limited availability of early-stage biopsy specimens and the inability of standard detection methods to capture low-abundance or spatially restricted viral antigens.[79] Previous research in transgenic mouse models and liver biopsies from HCV-infected individuals demonstrated a shift in HCV-driven metabolic zonation from the periportal domain towards the midlobular region and suggested that viral replication may preferentially occur in periportal hepatocytes.[94] The periportal enrichment of ISGs observed in tree shrew livers following HCV RNA inoculation is consistent with these findings and may reflect the initial hepatic entry point or early viral activity. Given that blood flow from the portal vein and hepatic artery enters the liver via the portal triads, the periportal region represents a frontline interface with circulating microbial and viral components. Immune cells enriched in this region are thus strategically positioned to mount rapid responses to invading pathogens.[95,96] It is plausible that initial sensing of HCV RNA occurred in periportal hepatocytes due to liver's unique blood flow, triggering a localised IFN response in tree shrew livers. Paracrine IFN signaling then activated adjacent cells and amplified ISG expression zonally. This speculation would be consistent with the "bystander effects" in HCV models.[97] Following this thread, localised induction of ISGs in periportal hepatocytes may function as an antiviral barrier, limiting viral spread and mitigating potential damage to cells near the central vein. Note that periportal hepatocytes being a potential "antiviral barrier" for HCV infection was also relevant to ano-rectal mucosal exposure and might not directly apply to infections initiated via other parenteral exposures. Future studies utilising the tree shrew model, with a controlled route of inoculation, might be helpful to uncover the influence of the initial hepatic engagement site on the establishment and subsequent spontaneous clearance of viral infection. Comprehensive spatial transcriptomic profiling will provide cell type-specific information to better understand the zonal expression patterns of ISGs in diverse hepatic cells.

Clinical and experimental evidence has long implicated HCV infection in the disruption of host glucose metabolism, with epidemiological studies linking chronic HCV to increased susceptibility to diabetes.[98] Viral proteins have been shown to interfere with glucose metabolism by modulating insulin signaling pathways.[99] Hepatic glucose production is tightly regulated by the balance between gluconeogenesis and glycolysis—pathways that were transcriptionally dysregulated in both liver tissues and cultured hepatic cells from tree shrews following HCV infection. These changes coincided with reductions in serum glucose and culture medium glucose levels (Fig. 3D and E), reflecting a systemic and cell-autonomous shift in metabolic activity. In contrast, HCV-infected Huh7 cells did not exhibit comparable alterations in glucose handling. Instead, perturbation of glycolytic flux in this human cell line facilitated viral replication, consistent with prior findings that HCV actively exploits host glucose metabolism to support its replication cycle.[100–103] In tree shrews, suppression of glucose and amino acid metabolism may serve a protective function by

reallocating metabolic resources toward IFN synthesis and the activation of antiviral programs, an energetically demanding but essential process during viral challenge.[104] This metabolic reprogramming likely represents an intrinsic antiviral strategy adopted by tree shrew hepatocytes to counteract HCV replication.

The single-cell transcriptomic atlas of tree shrew liver provides a powerful framework to dissect cell-type-specific responses and intercellular interactions following HCV RNA inoculation. Among the most striking findings was the emergence of a robust erythroblast population in the liver at the acute stage of inoculation (Fig. 4), highlighting a previously unrecognised perspective on the mechanisms of HCV infection. Erythroblasts are present in the bone marrow in healthy adult individuals and are abundantly found in neonates, cord blood, and placental tissue.[69,105] Under pathological conditions, such as anaemia, malignancy, or systemic infection, erythroblasts can become enriched in extramedullary organs.[106] The hepatic erythroblasts observed in this study were unlikely to be artefacts of cell contamination during sampling, as intracardiac perfusion was performed prior to liver extraction and erythrocyte lysis steps were incorporated to eliminate contaminating anucleate erythrocytes. Moreover, these cells exhibited robust expression of specific erythroid lineage markers (Fig. 4B), confirming their identity. Beyond their role in erythropoiesis, erythroblasts have increasingly been recognised as immunoregulatory cells.[72] For example, stress erythropoiesis with immunosuppressive features has been reported in infections with SARS-CoV-2, rotavirus, and respiratory syncytial virus.[107–109] Erythroblasts can also enhance the permissibility of $CD4^+$ T cells to HIV infection.[110] Additionally, HCV has been shown to infect $CD34^+$ haematopoietic progenitors, suggesting a potential haematologic viral reservoir in chronically infected carriers.[111] In the present study, hepatic erythroblasts expressed ISGs and exhibited extensive cell-cell interactions with hepatocytes and immune cells. TFR-mediated interactions, specifically TFRC and TFR2 binding to TF, along with LGALS9-P4HB and LGALS9-HAVCR2 signalling between erythroblasts and immune cells, suggested that erythroblasts were actively involved in the hepatic microenvironment during HCV infection. Notably, the TFR expressed in erythroblasts has been identified as a specific receptor of HCV E1/E2, with implications in facilitating viral entry.[112] Erythroblasts also contribute to systemic iron homeostasis by regulating iron influx and efflux, a function that may account for the observed upregulation of TFR and hepatic iron accumulation in patients with chronic hepatitis C infection.[113–115] Their interaction with hepatic immune cells in HCV-inoculated tree shrews suggests a potential immunosuppressive role, possibly serving to attenuate excessive immune activation and minimise tissue damage.[72] Therefore, targeting intrahepatic erythroblasts may represent a promising therapeutic strategy for mitigating inflammation and preventing the progression of chronic HCV infection.

In many viral infections, elevated neutrophil abundance is associated with disease progression.[77] Traditionally viewed as short-lived responders during acute inflammation, neutrophils are now recognised as contributors to chronic immune activation.[76] In the present study, neutrophils were markedly enriched in tree shrew livers at both acute and long-term timepoints following HCV RNA inoculation. This sustained presence likely reflects ongoing recruitment to sites of chronic inflammation and continued formation of NETs.[116] Immunofluorescence staining confirmed persistent NET activity, suggesting a pathogenic role in the hepatic injury observed at 111 wpi. This finding also indicated that despite viral clearance, HCV inoculation might induce lasting molecular and cellular imprints in the liver even at 111 wpi, which was included specifically to assess prolonged histological and molecular consequences of prior HCV exposure and mirrored analogous human studies investigating post-DAAs liver disease. Notably, a recent study reported an absence of NET formation in hepatic myeloid cells in patients with HCV chronic infection.[31] This discrepancy may stem from differences in tissue sampling, as fine needle aspirates used in human studies[31] may not adequately capture localised NET formation, highlighting the advantage of the tree shrew model for comprehensive tissue-based analyses.

There were several limitations in this study. First, it remains uncertain whether the transcriptional alterations observed in hepatic cell populations were specifically induced by HCV RNA. Single-cell technologies in our study were unable to distinguish infected from uninfected hepatocytes, precluding a definitive link between viral RNA presence and molecular phenotypes. Future advances in viral RNA detection at the single-cell and single-molecule levels will be essential to resolve this issue, particularly to determine whether intrahepatic erythroblasts and hepatocytes harbour replicating virus and serve as a potential reservoir. Second, this study did not capture the full temporal dynamics of immune responses during acute inoculation. Inclusion of additional early timepoints will be critical for mapping the dynamic orchestration of hepatic immunity and for identifying the precise timing of effector T-cell infiltration, which typically occurs in the peripheral blood and liver of humans and chimpanzees at 8–12 wpi.[26] A longitudinal analysis of immune cell populations in tree shrew livers would be instrumental in fully characterising this process. Moreover, we only used female tree shrews for infection in this study, and it remains to be determined whether there is a gender effect on the immune response in these tree shrews upon HCV acute inoculation. Third, the functional properties of erythroblasts in HCV inoculation remain

incompletely defined. The emergence of erythroblasts seemed to be related to innate immune response to some types of viruses including SARS-CoV-2, rotavirus, respiratory syncytial virus, and HIV, not only HCV. While transcriptional evidence suggested roles in iron homeostasis and immunoregulation, experimental validation using modified HCV RNAs (e.g., replication-defective mutants) through targeted functional assays is needed to clarify their contribution to viral restriction, immunosuppression, and iron metabolism within the infected liver.

In summary, this study integrated scRNA-seq and snRNA-seq to construct a detailed transcriptional map of tree shrew livers following acute and long-term HCV RNA inoculation. Through comprehensive cellular and molecular analyses, this study identified distinct immune and metabolic responses across hepatocytes, erythroblasts, and neutrophils. These findings not only advance our understanding of hepatic host-pathogen interactions during HCV challenge but also offer valuable insights for optimising the tree shrew as a preclinical model for viral hepatitis research.

Contributors

Y.-G.Y., D.Y., and J.Z. conceptualised the study. D.Y. and Y.-H.M. performed the infection experiments. D.Y. performed related cellular assays and tissue analyses. W.-B.K. and D.Y. analyzed and visualised the single cell sequencing data, and S.L., S.Z. and L.T. verified the underlying data. L.-B.L. contributed resources. D.Y. and Y.-G.Y. wrote the manuscript. J.Z., S.Z., S.L., and L.T. revised the manuscript. All authors approved the final version of the manuscript.

Data sharing statement

The raw sequencing data reported in this study comprise bulk RNA-seq, scRNA-seq, and snRNA-seq datasets deposited in the National Genomics Data Center (NGDC) under accession code PRJCA038250. These data are publicly accessible through the URL: https://ngdc.cncb.ac.cn/bioject/browse/PRJCA038250. The other data reported in this paper and any additional information will be shared by the lead contact upon reasonable request.

Declaration of interests

The authors declare that they have no competing interests.

Acknowledgements

This work was supported by grants from National Natural Science Foundation of China (U1902215, U25A20646), National Key Research and Development Plan Program (2022YFF0710900), Key Project of the CAS "Light of West China" Program (xbzg-zdsys-202302), and Yunnan Province (202305AH340006, 202001AS070023).

Appendix A. Supplementary data

Supplementary data related to this article can be found at https://doi.org/10.1016/j.ebiom.2025.106080.

References

1 World Health Organization. Global hepatitis report 2024: action for access in low- and middle-income countries pp 14-19 https://www.who.int/publications/i/item/9789240091672; 2024.
2 Ding Q, von Schaewen M, Ploss A. The impact of hepatitis C virus entry on viral tropism. *Cell Host Microbe*. 2014;16(5):562–568.
3 Maheshwari A, Ray S, Thuluvath PJ. Acute hepatitis C. *Lancet*. 2008;372(9635):321–332.
4 Chisari FV. Unscrambling hepatitis C virus-host interactions. *Nature*. 2005;436(7053):930–932.
5 Dore GJ, Feld JJ. Hepatitis C virus therapeutic development: in pursuit of "perfectovir". *Clin Infect Dis*. 2015;60(12):1829–1836.
6 Polaris Observatory HCV Collaborators. Global change in hepatitis C virus prevalence and cascade of care between 2015 and 2020: a modelling study. *Lancet Gastroenterol Hepatol*. 2022;7(5):396–415.
7 Roingeard P, Beaumont E. Hepatitis C vaccine: 10 good reasons for continuing. *Hepatology*. 2020;71(5):1845–1850.
8 Ploss A, Kapoor A. Animal models of hepatitis C virus infection. *Cold Spring Harb Perspect Med*. 2020;10(5):a036970.
9 Bukh J. A critical role for the chimpanzee model in the study of hepatitis C. *Hepatology*. 2004;39(6):1469–1475.
10 von Schaewen M, Ploss A. Murine models of hepatitis C: what can we look forward to? *Antiviral Res*. 2014;104:15–22.
11 Yao YG, Lu L, Ni RJ, et al. Study of tree shrew biology and models: a booming and prosperous field for biomedical research. *Zool Res*. 2024;45(4):877–909.
12 Fan Y, Ye MS, Zhang JY, et al. Chromosomal level assembly and population sequencing of the Chinese tree shrew genome. *Zool Res*. 2019;40(6):506–521.
13 Ye MS, Zhang JY, Yu DD, et al. Comprehensive annotation of the Chinese tree shrew genome by large-scale RNA sequencing and long-read isoform sequencing. *Zool Res*. 2021;42(6):692–709.
14 Zhao X, Tang ZY, Klumpp B, et al. Primary hepatocytes of *Tupaia belangeri* as a potential model for hepatitis C virus infection. *J Clin Invest*. 2002;109(2):221–232.
15 Feng Y, Feng YM, Lu C, et al. Tree shrew, a potential animal model for hepatitis C, supports the infection and replication of HCV *in vitro* and *in vivo*. *J Gen Virol*. 2017;98(8):2069–2078.
16 Tong Y, Zhu Y, Xia X, et al. Tupaia CD81, SR-BI, claudin-1, and occludin support hepatitis C virus infection. *J Virol*. 2011;85(6):2793–2802.
17 Xie ZC, Riezu-Boj JI, Lasarte JJ, et al. Transmission of hepatitis C virus infection to tree shrews. *Virology*. 1998;244(2):513–520.
18 Kayesh MEH, Ezzikouri S, Sanada T, et al. Oxidative stress and immune responses during hepatitis C virus infection in *Tupaia belangeri*. *Sci Rep*. 2017;7(1):9848.
19 Amako Y, Tsukiyama-Kohara K, Katsume A, et al. Pathogenesis of hepatitis C virus infection in *Tupaia belangeri*. *J Virol*. 2010;84(1):303–311.
20 Tian ZF, Shen H, Fu XH, et al. Interaction of hepatitis C virus envelope glycoprotein E2 with the large extracellular loop of *tupaia* CD81. *World J Gastroenterol*. 2009;15(2):240–244.
21 Barth H, Cerino R, Arcuri M, et al. Scavenger receptor class B type I and hepatitis C virus infection of primary *tupaia* hepatocytes. *J Virol*. 2005;79(9):5774–5785.
22 Xu L, Yu D, Yao YL, et al. *Tupaia* MAVS is a dual target during hepatitis C virus infection for innate immune evasion and viral replication via NF-κB. *J Immunol*. 2020;205(8):2091–2099.
23 Xu X, Chen H, Cao X, Ben K. Efficient infection of tree shrew (*Tupaia belangeri*) with hepatitis C virus grown in cell culture or from patient plasma. *J Gen Virol*. 2007;88(Pt 9):2504–2512.
24 Lin P, Yan X, Jing S, et al. Single-cell and spatially resolved transcriptomics for liver biology. *Hepatology*. 2024;80(3):698–720.
25 Trefts E, Gannon M, Wasserman DH. The liver. *Curr Biol*. 2017;27(21):R1147–R1151.
26 Stuart JD, Salinas E, Grakoui A. Immune system control of hepatitis C virus infection. *Curr Opin Virol*. 2021;46:36–44.
27 Saviano A, Henderson NC, Baumert TF. Single-cell genomics and spatial transcriptomics: discovery of novel cell states and cellular interactions in liver physiology and disease biology. *J Hepatol*. 2020;73(5):1219–1230.
28 Xu J, Guo P, Hao S, et al. A spatiotemporal atlas of mouse liver homeostasis and regeneration. *Nat Genet*. 2024;56(5):953–969.
29 Guo PC, Zuo J, Huang KK, et al. Cell atlas of CCl_4-induced progressive liver fibrosis reveals stage-specific responses. *Zool Res*. 2023;44(3):451–466.
30 Chu AL, Schilling JD, King KR, Feldstein AE. The power of single-cell analysis for the study of liver pathobiology. *Hepatology*. 2021;73(1):437–448.
31 Cui A, Li B, Wallace MS, et al. Single-cell atlas of the liver myeloid compartment before and after cure of chronic viral hepatitis. *J Hepatol*. 2024;80(2):251–267.
32 Xu L, Yu D, Fan Y, Peng L, Wu Y, Yao YG. Loss of RIG-I leads to a functional replacement with MDA5 in the Chinese tree shrew. *Proc Natl Acad Sci U S A*. 2016;113(39):10950–10955.

33 Dobin A, Davis CA, Schlesinger F, et al. STAR: ultrafast universal RNA-seq aligner. *Bioinformatics*. 2013;29(1):15–21.
34 Love MI, Huber W, Anders S. Moderated estimation of fold change and dispersion for RNA-seq data with DESeq2. *Genome Biol*. 2014;15(12):550.
35 Martin M. Cutadapt removes adapter sequences from high-throughput sequencing reads. *EMBnet J*. 2011;17(1):10.
36 Fan Y, Huang ZY, Cao CC, et al. Genome of the Chinese tree shrew. *Nat Commun*. 2013;4:1426.
37 Liao Y, Smyth GK, Shi W. featureCounts: an efficient general purpose program for assigning sequence reads to genomic features. *Bioinformatics*. 2014;30(7):923–930.
38 Wolf FA, Angerer P, Theis FJ. SCANPY: large-scale single-cell gene expression data analysis. *Genome Biol*. 2018;19(1):15.
39 Wolock SL, Lopez R, Klein AM. Scrublet: computational identification of cell doublets in single-cell transcriptomic data. *Cell Syst*. 2019;8(4):281–291.e9.
40 Ma Q, Ma W, Song TZ, et al. Single-nucleus transcriptomic profiling of multiple organs in a rhesus macaque model of SARS-CoV-2 infection. *Zool Res*. 2022;43(6):1041–1062.
41 Guilliams M, Bonnardel J, Haest B, et al. Spatial proteogenomics reveals distinct and evolutionarily conserved hepatic macrophage niches. *Cell*. 2022;185(2):379–396.e38.
42 Zhou Y, Zhou B, Pache L, et al. Metascape provides a biologist-oriented resource for the analysis of systems-level datasets. *Nat Commun*. 2019;10(1):1523.
43 Griss J, Viteri G, Sidiropoulos K, Nguyen V, Fabregat A, Hermjakob H. ReactomeGSA – efficient multi-omics comparative pathway analysis. *Mol Cell Proteomics*. 2020;19(12):2115–2125.
44 Vento-Tormo R, Efremova M, Botting RA, et al. Single-cell reconstruction of the early maternal-fetal interface in humans. *Nature*. 2018;563(7731):347–353.
45 Liang Y, Kaneko K, Xin B, et al. Temporal analyses of postnatal liver development and maturation by single-cell transcriptomics. *Dev Cell*. 2022;57(3):398–414.e5.
46 Polański K, Young MD, Miao Z, Meyer KB, Teichmann SA, Park JE. BBKNN: fast batch alignment of single cell transcriptomes. *Bioinformatics*. 2020;36(3):964–965.
47 Cao J, Spielmann M, Qiu X, et al. The single-cell transcriptional landscape of mammalian organogenesis. *Nature*. 2019;566(7745):496–502.
48 Yu D, Long Y, Xu L, et al. Infectivity of SARS-CoV-2 and protection against reinfection in rats. *Zool Res*. 2022;43(6):945–948.
49 Xu L, Yu D, Xu M, et al. Primate-specific BTN3A2 protects against SARS-CoV-2 infection by interacting with and reducing ACE2. *EBioMedicine*. 2024;107:105281.
50 Zhang X, Yu D, Wu Y, et al. Establishment and transcriptomic features of an immortalized hepatic cell line of the Chinese tree shrew. *Appl Microbiol Biotechnol*. 2020;104(20):8813–8823.
51 Yu D, Wu Y, Xu L, et al. Identification and characterization of toll-like receptors (TLRs) in the Chinese tree shrew (*Tupaia belangeri chinensis*). *Dev Comp Immunol*. 2016;60:127–138.
52 Livak KJ, Schmittgen TD. Analysis of relative gene expression data using real-time quantitative PCR and the $2^{-\Delta\Delta Ct}$ method. *Methods*. 2001;25(4):402–408.
53 Kolykhalov AA, Agapov EV, Blight KJ, Mihalik K, Feinstone SM, Rice CM. Transmission of hepatitis C by intrahepatic inoculation with transcribed RNA. *Science*. 1997;277(5325):570–574.
54 Hong Z, Beaudet-Miller M, Lanford RE, et al. Generation of transmissible hepatitis C virions from a molecular clone in chimpanzees. *Virology*. 1999;256(1):36–44.
55 Yanagi M, Purcell RH, Emerson SU, Bukh J. Transcripts from a single full-length cDNA clone of hepatitis C virus are infectious when directly transfected into the liver of a chimpanzee. *Proc Natl Acad Sci U S A*. 1997;94(16):8738–8743.
56 Hiraga N, Imamura M, Tsuge M, et al. Infection of human hepatocyte chimeric mouse with genetically engineered hepatitis C virus and its susceptibility to interferon. *FEBS Lett*. 2007;581(10):1983–1987.
57 Wakita T. Cell culture systems of HCV using JFH-1 and other strains. *Cold Spring Harb Perspect Med*. 2019;9(11):a036806.
58 Andrews TS, Atif J, Liu JC, et al. Single-cell, single-nucleus, and spatial RNA sequencing of the human liver identifies cholangiocyte and mesenchymal heterogeneity. *Hepatol Commun*. 2022;6(4):821–840.
59 Oh JM, An M, Son DS, et al. Comparison of cell type distribution between single-cell and single-nucleus RNA sequencing: enrichment of adherent cell types in single-nucleus RNA sequencing. *Exp Mol Med*. 2022;54(12):2128–2134.
60 Bang BR, Elmasry S, Saito T. Organ system view of the hepatic innate immunity in HCV infection. *J Med Virol*. 2016;88(12):2025–2037.
61 Sularea VM, Sugrue JA, O'Farrelly C. Innate antiviral immunity and immunometabolism in hepatocytes. *Curr Opin Immunol*. 2023;80:102267.
62 Ling ZN, Jiang YF, Ru JN, Lu JH, Ding B, Wu J. Amino acid metabolism in health and disease. *Signal Transduct Target Ther*. 2023;8(1):345.
63 Morris SM Jr. Regulation of enzymes of the urea cycle and arginine metabolism. *Annu Rev Nutr*. 2002;22:87–105.
64 Lercher A, Bhattacharya A, Popa AM, et al. Type I interferon signaling disrupts the hepatic urea cycle and alters systemic metabolism to suppress T cell function. *Immunity*. 2019;51(6):1074–1087.e9.
65 Vieyres G, Reichert I, Carpentier A, Vondran FWR, Pietschmann T. The ATGL lipase cooperates with ABHD5 to mobilize lipids for hepatitis C virus assembly. *PLoS Pathog*. 2020;16(6):e1008554.
66 Petersen MC, Vatner DF, Shulman GI. Regulation of hepatic glucose metabolism in health and disease. *Nat Rev Endocrinol*. 2017;13(10):572–587.
67 Lin SC, Hardie DG. AMPK: sensing glucose as well as cellular energy status. *Cell Metab*. 2018;27(2):299–313.
68 Li K, Chen Z, Kato N, Gale M Jr, Lemon SM. Distinct poly(I-C) and virus-activated signaling pathways leading to interferon-beta production in hepatocytes. *J Biol Chem*. 2005;280(17):16739–16747.
69 Elahi S, Ertelt JM, Kinder JM, et al. Immunosuppressive CD71+ erythroid cells compromise neonatal host defence against infection. *Nature*. 2013;504(7478):158–162.
70 Zheng Z, He H, Tang XT, et al. Uncovering the emergence of HSCs in the human fetal bone marrow by single-cell RNA-seq analysis. *Cell Stem Cell*. 2022;29(11):1562–1579.e7.
71 Du J, Li Z, Gong Y, Lan Y, Liu B. Integrative cross-species transcriptome analysis reveals earlier occurrence of myelopoiesis in pre-circulation primates compared to mice. *Zool Res*. 2024;45(6):1276–1286.
72 Grzywa TM, Nowis D, Golab J. The role of CD71(+) erythroid cells in the regulation of the immune response. *Pharmacol Ther*. 2021;228:107927.
73 Bi S, Hong PW, Lee B, Baum LG. Galectin-9 binding to cell surface protein disulfide isomerase regulates the redox environment to enhance T-cell migration and HIV entry. *Proc Natl Acad Sci U S A*. 2011;108(26):10650–10655.
74 Lai JH, Luo SF, Wang MY, Ho LJ. Translational implication of galectin-9 in the pathogenesis and treatment of viral infection. *Int J Mol Sci*. 2017;18(10):2108.
75 Zhu C, Anderson AC, Schubart A, et al. The Tim-3 ligand galectin-9 negatively regulates T helper type 1 immunity. *Nat Immunol*. 2005;6(12):1245–1252.
76 Liew PX, Kubes P. The neutrophil's role during health and disease. *Physiol Rev*. 2019;99(2):1223–1248.
77 Rawat S, Vrati S, Banerjee A. Neutrophils at the crossroads of acute viral infections and severity. *Mol Aspects Med*. 2021;81:100996.
78 Papayannopoulos V. Neutrophil extracellular traps in immunity and disease. *Nat Rev Immunol*. 2018;18(2):134–147.
79 Liang Y, Shilagard T, Xiao SY, et al. Visualizing hepatitis C virus infections in human liver by two-photon microscopy. *Gastroenterology*. 2009;137(4):1448–1458.
80 Wieland S, Makowska Z, Campana B, et al. Simultaneous detection of hepatitis C virus and interferon stimulated gene expression in infected human liver. *Hepatology*. 2014;59(6):2121–2130.
81 Graw F, Balagopal A, Kandathil AJ, et al. Inferring viral dynamics in chronically HCV infected patients from the spatial distribution of infected hepatocytes. *PLoS Comput Biol*. 2014;10(11):e1003934.
82 Lee J, Ou JHJ. Hepatitis C virus and intracellular antiviral response. *Curr Opin Virol*. 2022;52:244–249.
83 Liang Y, Cao X, Ding Q, Zhao Y, He Z, Zhong J. Hepatitis C virus NS4B induces the degradation of TRIF to inhibit TLR3-mediated interferon signaling pathway. *PLoS Pathog*. 2018;14(5):e1007075.
84 Cao X, Ding Q, Lu J, et al. MDA5 plays a critical role in interferon response during hepatitis C virus infection. *J Hepatol*. 2015;62(4):771–778.
85 Du X, Pan T, Xu J, et al. Hepatitis C virus replicative double-stranded RNA is a potent interferon inducer that triggers

interferon production through MDA5. *J Gen Virol*. 2016;97(11):2868–2882.
86 Hei L, Zhong J. Laboratory of genetics and physiology 2 (LGP2) plays an essential role in hepatitis C virus infection-induced interferon responses. *Hepatology*. 2017;65(5):1478–1491.
87 Wong MT, Chen SS. Emerging roles of interferon-stimulated genes in the innate immune response to hepatitis C virus infection. *Cell Mol Immunol*. 2016;13(1):11–35.
88 Xu Y, Zhong J. Innate immunity against hepatitis C virus. *Curr Opin Immunol*. 2016;42:98–104.
89 Su AI, Pezacki JP, Wodicka L, et al. Genomic analysis of the host response to hepatitis C virus infection. *Proc Natl Acad Sci U S A*. 2002;99(24):15669–15674.
90 Bigger CB, Brasky KM, Lanford RE. DNA microarray analysis of chimpanzee liver during acute resolving hepatitis C virus infection. *J Virol*. 2001;75(15):7059–7066.
91 Marukian S, Andrus L, Sheahan TP, et al. Hepatitis C virus induces interferon-lambda and interferon-stimulated genes in primary liver cultures. *Hepatology*. 2011;54(6):1913–1923.
92 Schoggins JW. Interferon-stimulated genes: what do they all do? *Annu Rev Virol*. 2019;6(1):567–584.
93 Jungermann K, Kietzmann T. Zonation of parenchymal and nonparenchymal metabolism in liver. *Annu Rev Nutr*. 1996;16:179–203.
94 Moreau M, Rivière B, Vegna S, et al. Hepatitis C viral proteins perturb metabolic liver zonation. *J Hepatol*. 2015;62(2):278–285.
95 Gola A, Dorrington MG, Speranza E, et al. Commensal-driven immune zonation of the liver promotes host defence. *Nature*. 2021;589(7840):131–136.
96 Miyamoto Y, Kikuta J, Matsui T, et al. Periportal macrophages protect against commensal-driven liver inflammation. *Nature*. 2024;629(8013):901–909.
97 Sheahan T, Imanaka N, Marukian S, et al. Interferon lambda alleles predict innate antiviral immune responses and hepatitis C virus permissiveness. *Cell Host Microbe*. 2014;15(2):190–202.
98 Ding Y, Li G, Zhou Z, Deng T. Molecular mechanisms underlying hepatitis C virus infection-related diabetes. *Metabolism*. 2021;121:154802.
99 Leslie J, Geh D, Elsharkawy AM, Mann DA, Vacca M. Metabolic dysfunction and cancer in HCV: shared pathways and mutual interactions. *J Hepatol*. 2022;77(1):219–236.
100 Lupberger J, Croonenborghs T, Roca Suarez AA, et al. Combined analysis of metabolomes, proteomes, and transcriptomes of hepatitis C virus-infected cells and liver to identify pathways associated with disease development. *Gastroenterology*. 2019;157(2):537–551.e9.
101 Yu T, Yang Q, Tian F, et al. Glycometabolism regulates hepatitis C virus release. *PLoS Pathog*. 2021;17(7):e1009746.
102 Shlomai A, Rechtman MM, Burdelova EO, et al. The metabolic regulator PGC-1alpha links hepatitis C virus infection to hepatic insulin resistance. *J Hepatol*. 2012;57(4):867–873.
103 Deng L, Shoji I, Ogawa W, et al. Hepatitis C virus infection promotes hepatic gluconeogenesis through an NS5A-mediated, FoxO1-dependent pathway. *J Virol*. 2011;85(17):8556–8568.
104 Šestan M, Mikašinović S, Benić A, et al. An IFNγ-dependent immune-endocrine circuit lowers blood glucose to potentiate the innate antiviral immune response. *Nat Immunol*. 2024;25(6):981–993.
105 Dunsmore G, Bozorgmehr N, Delyea C, Koleva P, Namdar A, Elahi S. Erythroid suppressor cells compromise neonatal immune response against *Bordetella pertussis*. *J Immunol*. 2017;199(6):2081–2095.
106 Zhao L, He R, Long H, et al. Late-stage tumors induce anemia and immunosuppressive extramedullary erythroid progenitor cells. *Nat Med*. 2018;24(10):1536–1544.
107 Shahbaz S, Xu L, Osman M, et al. Erythroid precursors and progenitors suppress adaptive immunity and get invaded by SARS-CoV-2. *Stem Cell Reports*. 2021;16(5):1165–1181.
108 Yang L, Shivakumar P, Kinder J, et al. Regulation of bile duct epithelial injury by hepatic CD71+ erythroid cells. *JCI Insight*. 2020;5(11):e135751.
109 Rinchai D, Altman MC, Konza O, et al. Definition of erythroid cell-positive blood transcriptome phenotypes associated with severe respiratory syncytial virus infection. *Clin Transl Med*. 2020;10(8):e244.
110 Namdar A, Dunsmore G, Shahbaz S, et al. CD71(+) erythroid cells exacerbate HIV-1 susceptibility, mediate trans-infection, and harbor infective viral particles. *mBio*. 2019;10(6):e02767-19.
111 Sansonno D, Lotesoriere C, Cornacchiulo V, et al. Hepatitis C virus infection involves CD34(+) hematopoietic progenitor cells in hepatitis C virus chronic carriers. *Blood*. 1998;92(9):3328–3337.
112 Martin DN, Uprichard SL. Identification of transferrin receptor 1 as a hepatitis C virus entry factor. *Proc Natl Acad Sci U S A*. 2013;110(26):10777–10782.
113 Zou DM, Sun WL. Relationship between hepatitis C virus infection and iron overload. *Chin Med J (Engl)*. 2017;130(7):866–871.
114 Saito H, Fujimoto Y, Ohtake T, et al. Up-regulation of transferrin receptor 1 in chronic hepatitis C: implication in excess hepatic iron accumulation. *Hepatol Res*. 2005;31(4):203–210.
115 Takeo M, Kobayashi Y, Fujita N, et al. Upregulation of transferrin receptor 2 and ferroportin 1 mRNA in the liver of patients with chronic hepatitis C. *J Gastroenterol Hepatol*. 2005;20(4):562–569.
116 Castanheira FVS, Kubes P. Neutrophils and NETs in modulating acute and chronic inflammation. *Blood*. 2019;133(20):2178–2185.

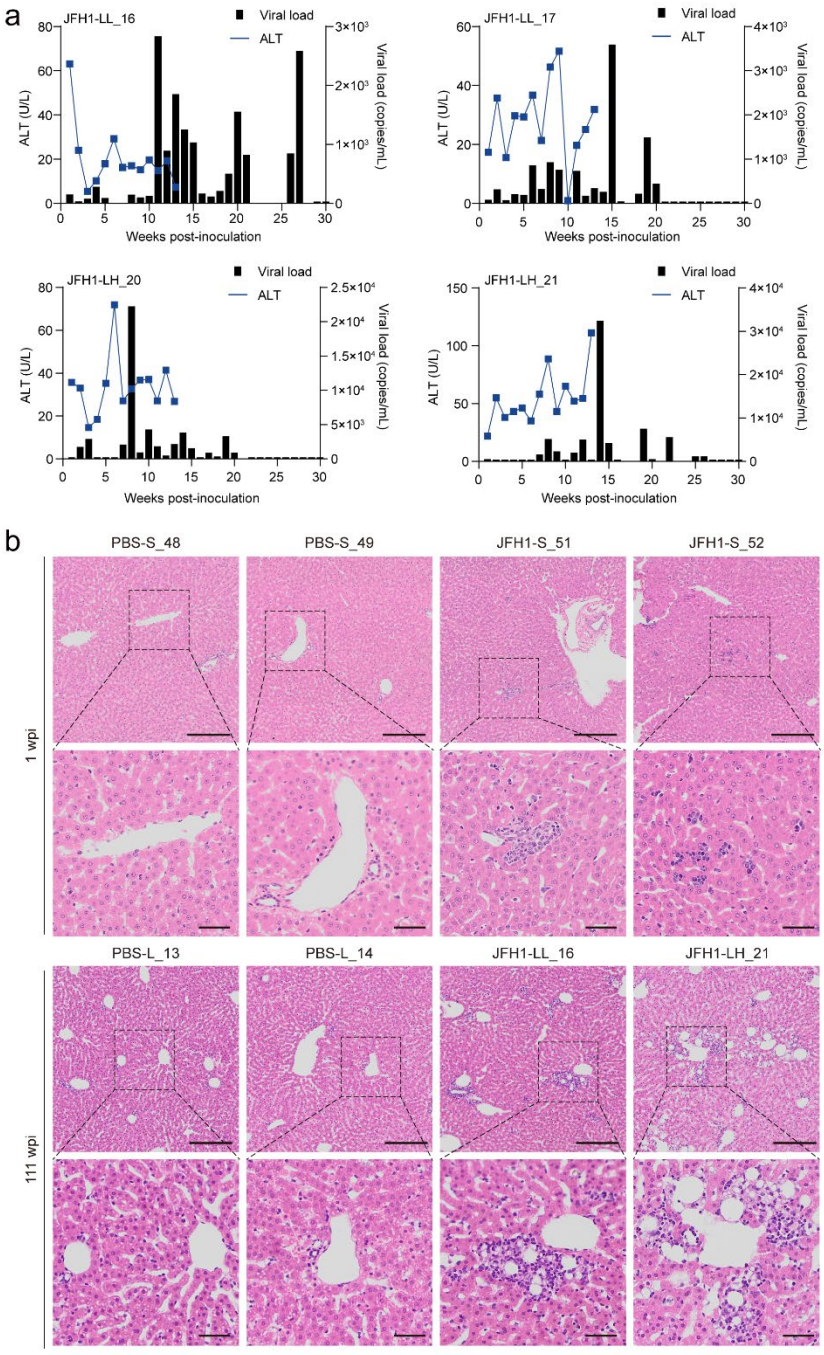

Supplementary Fig. 1: Viral load, serum ALT, and pathological changes in tree shrews inoculated with HCV RNA. (a) HCV viral load and serum ALT concentrations in tree shrews with long-term inoculation of HCV RNA. Curved line and left ordinates represent serum ALT concentrations (U/L serum), and bars and right ordinates represent HCV RNA (copies/mL of serum). (b) Representative H&E-stained images of tree shrew liver tissues at 1 wpi (*upper*) and 111 wpi (bottom). Magnified images refer to indicated boxed areas. Scale bar, 200 μm for liver section and 50 μm for enlarged view of boxed areas.

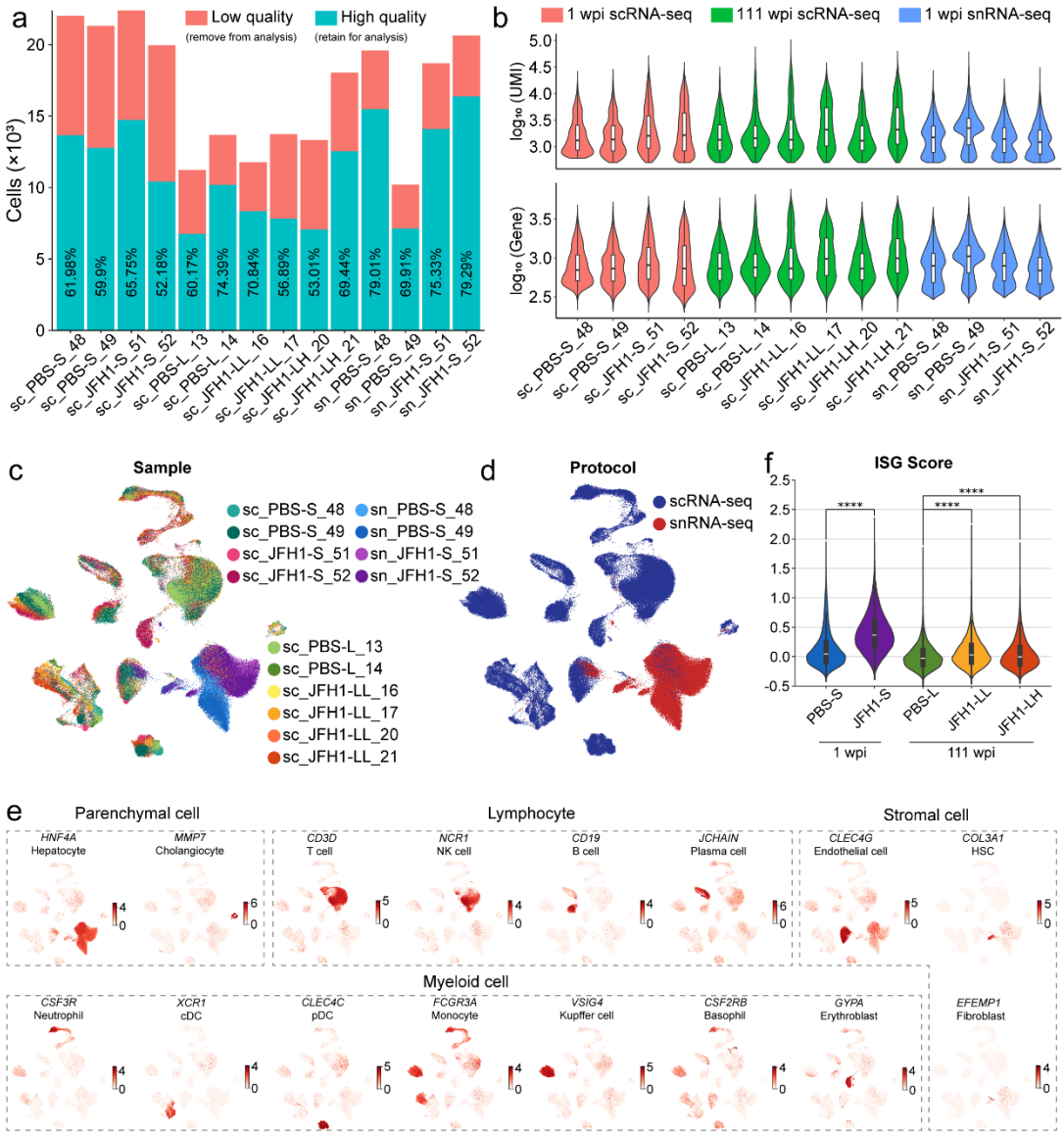

Supplementary Fig. 2: Quality evaluation and comparison of cells captured by scRNA-seq and snRNA-seq. (a) Stacked bar graph showing total cell counts in each sample. Percentages represent proportions of high-quality cells used for subsequent analyses. Prefixes "sc" and "sn" in sample ID indicate data obtained by scRNA-seq and snRNA-seq, respectively. (b) Violin plot showing $\log_{10}$ of UMI counts per cell (*upper*) and $\log_{10}$ gene counts per cell (*lower*) in each sample. (c) UMAP visualization of cell types, colored by individual samples. (d) UMAP visualization of cell types, colored by capture protocol (scRNA-seq and snRNA-seq). (e) UMAP visualization showing expression of marker genes for all 16 major cell types defined in Fig. 1c. (f) Violin plot showing ISG score for all liver cells from tree shrews with acute (PBS-S vs. JFH1-S) and long-term (PBS-L vs. JFH1-LL or JFH1-LH) inoculation of HCV RNA. Statistical significance was assessed by the Kruskal-Wallis test followed by Dunnett's multiple comparisons test, ****, $P < 0.0001$.

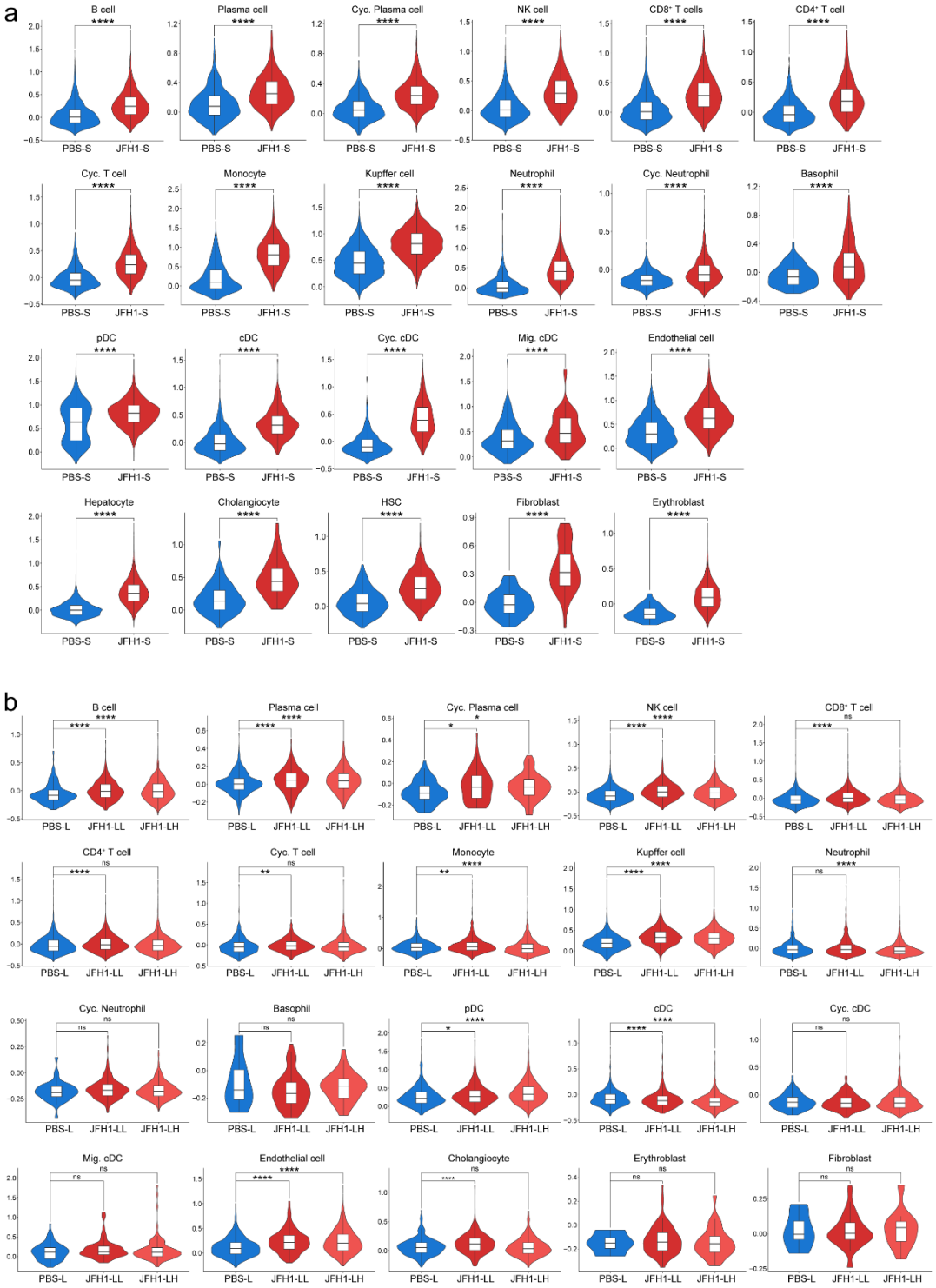

Supplementary Fig. 3: HCV inoculation induces ISG expression in tree shrew liver cells. Violin plots showing ISG score of each cell type in tree shrew livers at 1 wpi (a) and at 111 wpi (b). The Wilcoxon rank sum test for (a) and the Kruskal-Wallis test followed by Dunnett's multiple comparisons test for (b) were used for statistical analyses. ns, not significant; *, $P < 0.05$; **, $P < 0.01$; ***, $P < 0.001$; ****, $P < 0.0001$.

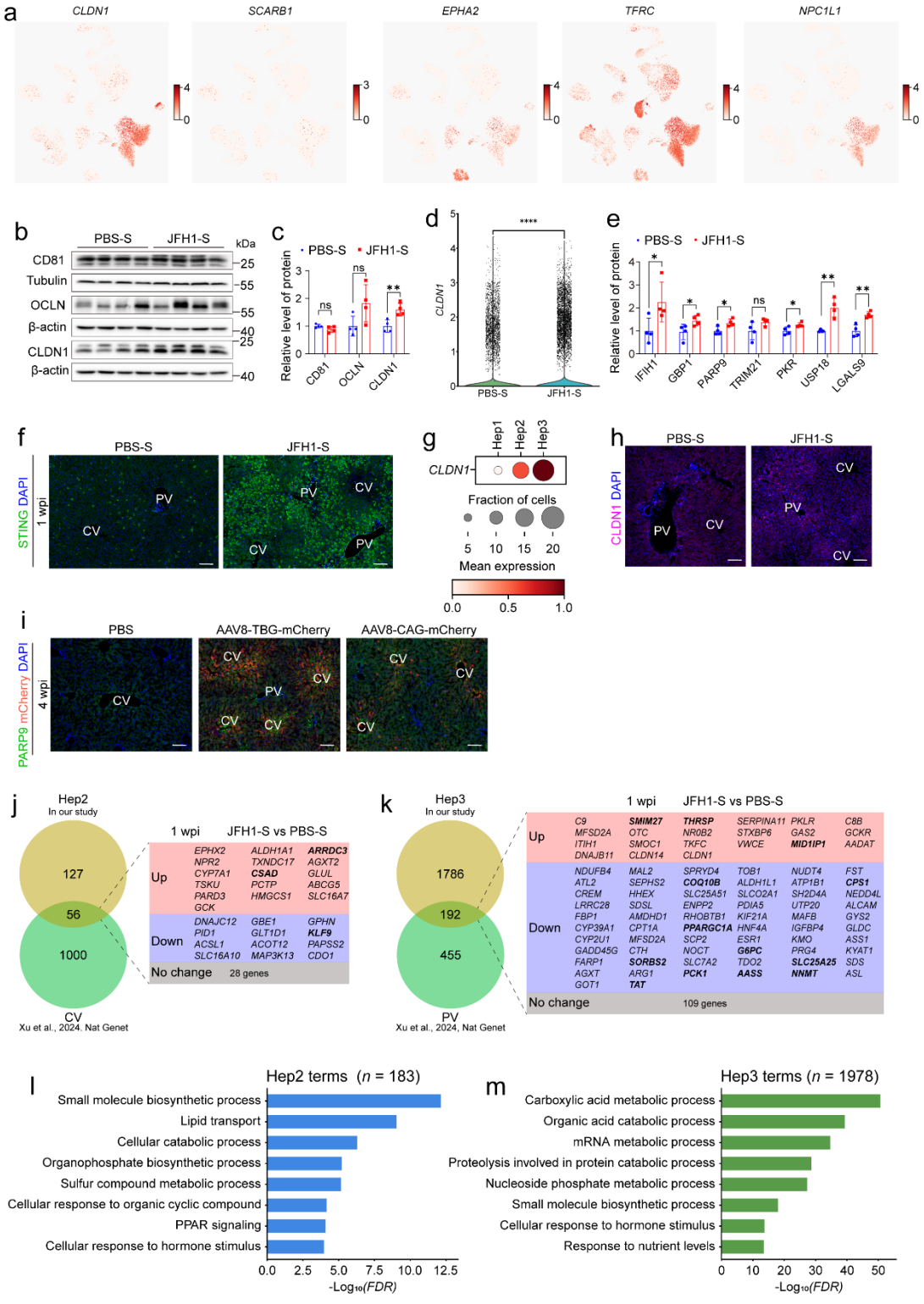

Supplementary Fig. 4. Expression of HCV entry factors and ISG zonation in tree shrew livers. (a) UMAP visualization showing cells expressing genes involved in HCV entry (*CLDN1*, *SCARB1*, *EPHA2*, *TFRC*, and *NPC1L1*). Cells expressing respective genes are scaled in red. (b-c) The protein levels of CD81, OCLN, and CLDN1 in liver tissues from PBS-S and JFH1-S groups (b) and the related

quantitative analysis (c). (d) Violin plot showing expression of *CLDN1* between PBS-S and JFH1-S groups at 1 wpi. (e) The protein levels of representative ISGs in tree shrew livers from PBS-S and JFH1-S groups were quantified, related to Fig. 2g. (f) Representative immunofluorescence images of STING (*green*) and DAPI (*blue*) in liver tissues from tree shrews at 1 wpi. (g) Dot plot indicating relative expression of CLDN1 in three hepatocyte subclusters. Size of circle indicates percentage of cells in each population, with color scale showing average expression level. (h) Representative immunofluorescence images of CLDN1 (*magenta*) and DAPI (*blue*) in liver tissues from tree shrews at 1 wpi. (i) Representative immunofluorescence images of mCherry (*red*), PARP9 (*green*), and DAPI (*blue*) in liver tissues from tree shrews with AAV8 infection (4 wpi). Scale bars in (f, h, i), 100 μm; PV, portal vein; CV, central vein. (j–k) Identification of genes in hepatocytes with zonated expression affected by HCV inoculation. Venn diagram showing number of overlapping DEGs in tree shrew Hep2 in this study ($\log_2$ (fold change) > 0.5, FDR < 1×10^{-5}), CV genes in mouse hepatocytes (FDR < 1×10^{-5}) reported by Xu et al. [1] (j), and DEGs in tree shrew Hep3 in this study and PV genes in mouse hepatocytes (k). Zone-specific genes are listed as upregulated or downregulated ($|\log_2$ (fold change)| > 0.5, FDR < 1×10^{-5}) in hepatocytes between PBS-S and JFH1-S groups using different shadowed colors. Sixteen genes (names in bold) showed significant expressional change in bulk RNA isolated from whole liver tissues in JFH1-S group compared to PBS-S group ($|\log_2$ (fold change)| > 1, FDR < 0.05). (l–m) Functional enrichment analyses of Hep2- (l) and Hep3- (m) DEGs in JFH1-S groups ($\log_2$ (fold change) > 0.5, FDR < 1×10^{-5}). Data in (c and e) are presented as mean ± SD. Two-tailed unpaired Student's *t*-test was used for (c, e, $n = 4$ animals per group). Wilcoxon rank-sum test was used for (d). ns, not significant; *, $P < 0.05$; **, $P < 0.01$. ****, $P < 0.0001$.

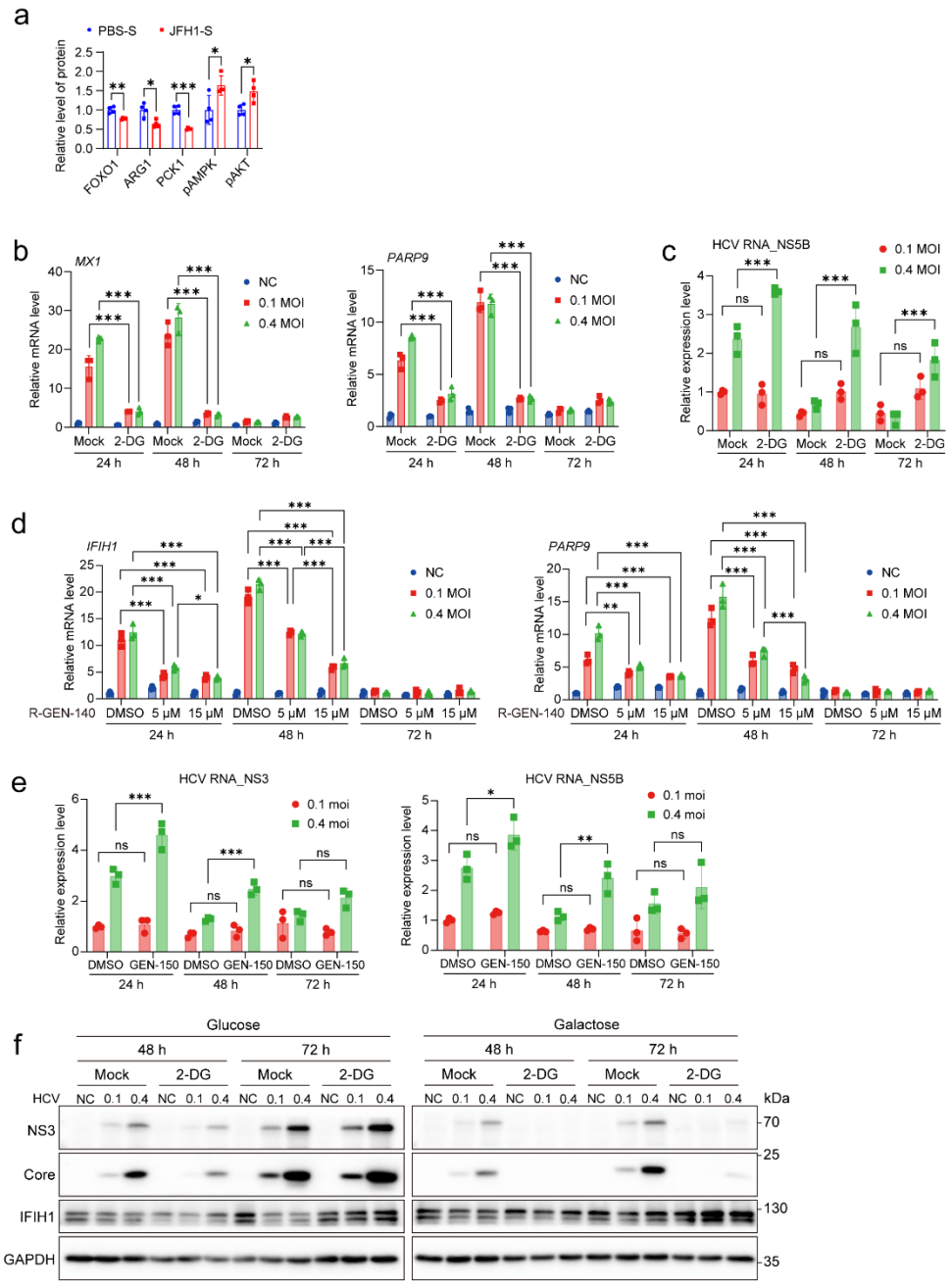

Supplementary Fig. 5: HCV infection disrupts glucose metabolism and innate immune responses in tree shrew ITH6 cells and human Huh7 cells. (a) The protein levels of FOXO1, ARG1, PCK1, pAMPK, and pAKT in tree shrew livers from PBS-S and JFH1-S groups were quantified, related to Fig. 3c. (b) mRNA expression level of *MX1* and *PARP9* in ITH6 cells with or without 2-DG treatment. ITH6 cells were infected with HCV at MOIs of 0.1 or 0.4 for 6 h, then switched to culture medium supplemented with 2-DG (2 mM). Cells were harvested at 24, 48, and 72 hpi for qRT-PCR. (c) Quantification of intracellular HCV RNAs in ITH6 cells with or without 2-DG treatment (2 mM) for indicated timepoints after HCV infection. Cells were treated

under the same conditions in (b). HCV genomic NS5B gene (HCV RNA_NS5B) was detected by qRT-PCR. (d) mRNA levels of *IFIH1* and *PARP9* in ITH6 cells with or without R-GEN-140 treatment. ITH6 cells were infected with HCV at MOIs of 0.1 or 0.4 for 6 h, then switched to culture medium supplemented with R-GEN-140 (5 μM and 15 μM). Cells were harvested at 24, 48, and 72 hpi for qRT-PCR. (e) Quantification of intracellular HCV RNAs in ITH6 cells with or without R-GEN-140 treatment in (d). HCV RNAs were measured by qRT-PCR for HCV genomic NS3 gene (HCV RNA_NS3) and genomic NS5B gene (HCV RNA_NS5B), respectively. (f) Protein levels of HCV proteins (NS3 and Core) and IFIH1 in Huh7 cells with and without 2-DG treatment. Huh7 cells were cultured in glucose and galactose media, respectively, then infected with HCV at MOIs of 0.1 or 0.4 for 6 h. Cells were then switched to culture medium supplemented with 2-DG (2 mM). Cells were harvested at 48 and 72 hpi for immunoblotting. Data are presented as mean ± SD. Two-tailed unpaired Student's *t*-test was used for (a), $n = 4$ animals per group. Two-way ANOVA with Tukey's multiple comparisons test was used for (b, c, d, and e). $n = 3$ biological replicates. ns, not significant; *$P < 0.05$; ** $P < 0.01$; *** $P < 0.001$.

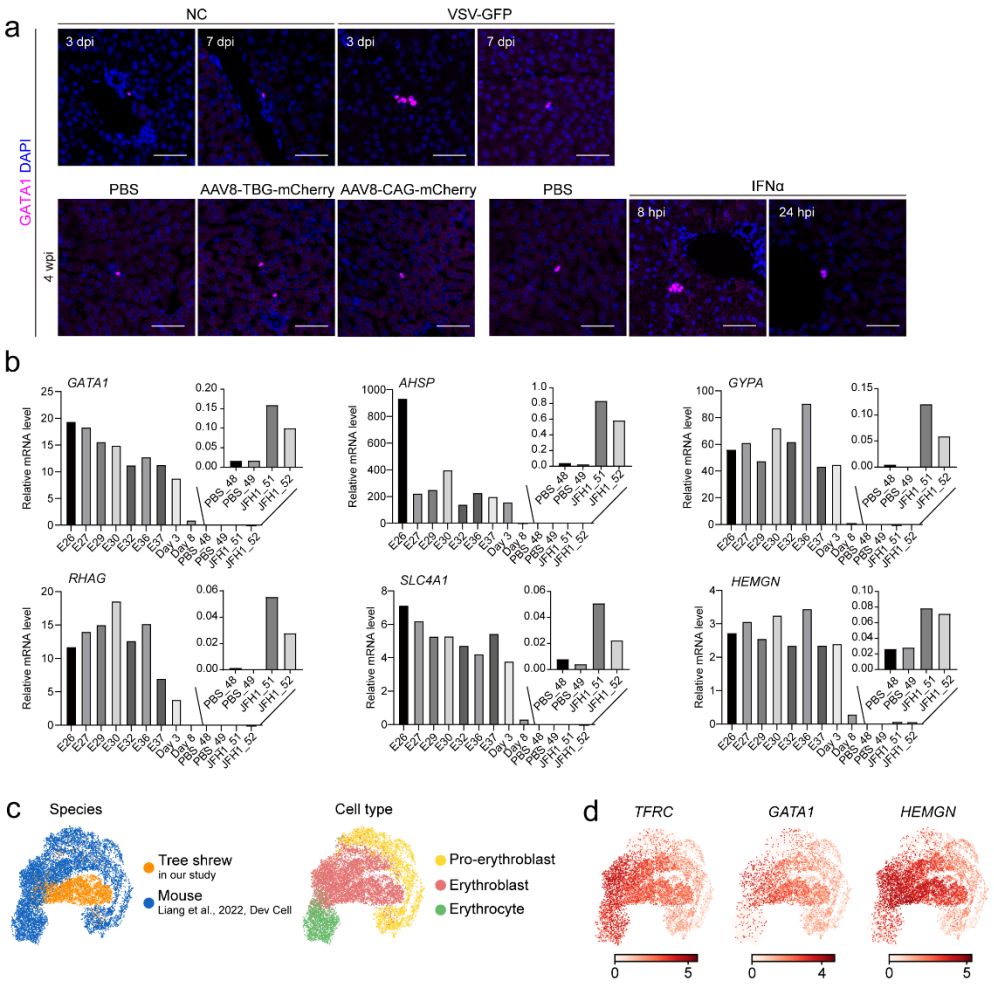

Supplementary Fig. 6: Expression levels of representative erythroid marker genes in tree shrew embryos and livers compared to mice. (a) Representative immunofluorescence images of GATA1 (*magenta*) and DAPI (*blue*) in liver tissues from tree shrews following intravenous injection of VSV-GFP (3 dpi and 7 dpi), AAV8-mCherry (4 wpi), or IFNα (8 hpi and 24 hpi). Scale bar, 50 μm. (b) Relative mRNA expression level of representative erythroid lineage genes in tree shrew fetal liver, neonatal liver, and livers from animals at 1 wpi. Gene expression was detected by qRT-PCR and normalized to *β-actin*. Zoomed insets show liver samples at 1 wpi. (c) UMAP visualization of integrated erythroblasts in tree shrew livers following acute HCV inoculation and erythroid cells (pro-erythroblasts, erythroblasts, and erythrocytes) from single-cell transcriptome of mouse livers at postnatal days 1, 3, 7, 21, and 56. Cells are marked by species (*left*) and cell type (*right*). (d) UMAP visualization of erythroid cells, colored by expression of representative erythroid marker genes in tree shrews and mice. Mouse data in (c–d) were taken from reported research [2].

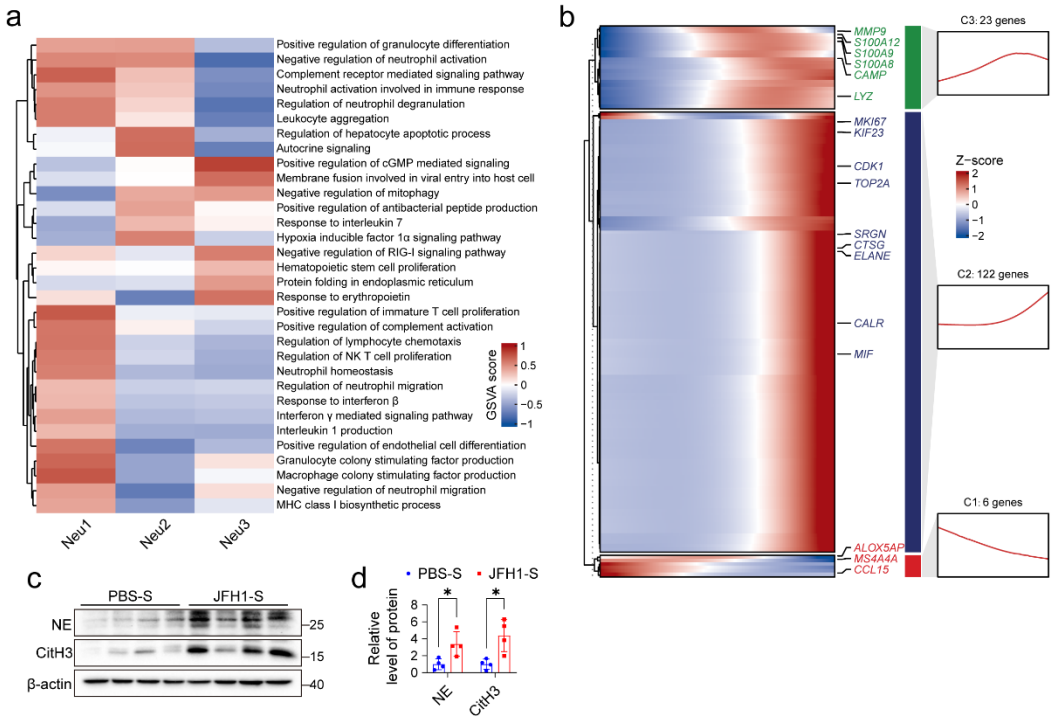

Supplementary Fig. 7: Neutrophil subclusters and functional enrichment in tree shrew livers. (a) Functional enrichment analysis of DEGs in each neutrophil subcluster. (b) Gene expression profiles of neutrophils ordered according to pseudo-time trajectory. Z scores of relative gene expression levels are displayed, with red representing higher and blue representing lower abundance. (c-d) Protein levels of NE and CitH3 in liver tissues from tree shrew livers from PBS-S and JFH1-S groups (c) and the related quantitative analysis (d), related to Fig. 5k. $n = 4$ animals that were used in the newly added experiments during the revision of this work. Two-tailed unpaired Student's *t*-test was used for (d). Data are presented as mean ± SD. $^*P < 0.05$.

Supplementary Table S1: Information of the tree shrews and viral infections in this study.

Number [a]	Animal ID	Sex	Age (days)	Time points	Groups	HCV RNA [b] or virus dose	Approach / Application
1	PBS-S_48	Female	75	7 days	PBS-S	-	Intrahepatic injection; scRNA-seq and snRNA-seq; validations
2	PBS-S_49	Female	70				
3	PBS-S_127	Female	89				
4	PBS-S_128	Female	89				
5	PBS-S_129	Female	89				
6	PBS-S_130	Female	89				
7	JFH1-S_51	Female	70	7 days	JFH1-S	30 μg	
8	JFH1-S_52	Female	87				
9	JFH1-S_132	Female	93				
10	JFH1-S_133	Female	92				
11	JFH1-S_137	Female	85				
12	JFH1-S_138	Female	85				
13	PBS-L_13	Male	55	111 weeks	PBS-L	-	Intrahepatic injection; scRNA-seq and validations
14	PBS-L_14	Male	65				
15	JFH1-LL_16	Female	57	111 weeks	JFH1-LL	10 μg	
16	JFH1-LL_17	Male	57				
17	JFH1-LH_20	Male	59	111 weeks	JFH1-LH	30 μg	
18	JFH1-LH_21	Female	61				
19	NC_101	Female	89	3 days	NC-3D [c]	-	Intravenous injection; validation
20	NC_102	Female	89				
21	NC_123	Female	78				
22	NC_103	Female	89	7 days	NC-7D	-	
23	NC_104	Female	89				

24	VSV_105	Female	75	3 days	VSV-3D	1×10^9 PFU	
25	VSV_106	Female	75				
26	VSV_122	Female	78				
27	VSV_107	Female	75	7 days	VSV-7D	1×10^9 PFU	
28	VSV_108	Female	75				
29	NC_119	Female	53	4 weeks	PBS [d]	-	
30	AAV8_117	Female	53	4 weeks	AAV8-TBG-mCherry	1×10^{12} GC	
31	AAV8_118	Female	53		AAV8-CAG-mCherry	1×10^{12} GC	
32	NC_111	Female	83	8 hours	PBS [d]	-	
33	NC_112	Female	83	24 hours	PBS [d]	-	
34	IFN_113	Female	78	8 hours	IFN-8h	2×10^5 U	
35	IFN_114	Female	78				
36	IFN_115	Female	79	24 hours	IFN-24h	2×10^5 U	
37	IFN_116	Female	79				
38	#53	-	3	-	-	-	Analysis of erythroid genes expression in tree shrew pups
39	#54	-	8	-	-	-	

[a] Animals number 3-6, 9-12, 21, 26, 32-37 were used in the newly added experiments during the revision of this work. [b] HCV RNA, *in vitro* transcribed RNAs corresponding to the full-length JFH1 genome; [c] NC-3D, an uninfected group received an injection containing only culture medium for 3 days; [d] PBS, an uninfected group injected with PBS for indicated timepoint.

Supplementary Table S2: Primers used for quantitative real-time PCR (qRT-PCR) in this study.

Gene	Name	Primer sequence (5' – 3')
For tree shrew		
tEIF2AK2	tEIF2AK2-F	CAGGAGTGGATTACATACATTC
	tEIF2AK2-R	TCGTTCGCTTCTCTTCAT
tPARP9	tPARP9-F	CTCAGTGCCCTGCGACCCA
	tPARP9-R	ACTTCCGCCTCAAACACGTA
tSTAT1	tSTAT1-F	GGCCCTCTCATTGTTACTG
	tSTAT1-R	TTGGGAGCTGGCTTACGTT
tIFIH1	tIFIH1-F	TTACAGGGCTCAACCATC
	tIFIH1-R	CATGCTTGACCACATTTG
tFOXO1	tFOXO1-F	TTATTGAGCGCTTGGACTGT
	tFOXO1-R	AGCTTTGGTTGGGCAACAC
tG6PC	tG6PC-F	TTCGGTTCCTGAACGTCCTT
	tG6PC-R	GGCCAGGTAGATTCGTGACA
tPCK1	tPCK1-F	GGTAACTTAAGGGCTATCAA
	tPCK1-R	GGTCTGAATGGCGTTAG
tARG1	tARG1-F	AAGTCAAGAAGAACGGGAGA
	tARG1-R	CCCAAATGACGCCAAGA
β-actin	tβ-actin-F	ATTTTGAATGATCAGCCACC
	tβ-actin-R	AGGTAAGCCCTGGCTGCCTC
tHK2	tHK2-F	GCCAAGGTCATGCGTGAGAC
	tHK2-R	CAGGCGACAGCAGTAATG
tPGK1	tPGK1-F	CCGCTTTCATGTAGAGG
	tPGK1-R	TTCTGTGGCAGATTGACTCC
tSLC2A1	tSLC2A1-F	ATGGCAAGCTGCGCTGTG
	tSLC2A1-R	CAAAGATGGCCACGATGCTC
tGYPA	tGYPA-F	GCTGGTATCATTGGAACTAT
	tGYPA-R	GCATTTCCTGTTTCAACG
tAHSP	tAHSP-F	GGCTCTGAATGAACTCCGT
	tAHSP-R	GGAAGGCAGTGGGTGAGTCA
tGATA1	tGATA1-F	CCCCAGTCTTTCAGGTGTAC
	tGATA1-R	GGGAGGAGAGTCTTCACGAG
tHEMGN	tHEMGN-F	GCCCTTCCTTCTACATCAT
	tHEMGN-R	CTGGGTTTTGGTAAGTGTCA
tRHAG	tRHAG-F	CATCTCTGTGTTTGGGTACA
	tRHAG-R	CCGTGCAGGTTATGGAC
tSLC4A1	tSLC4A1-F	ACCACCCGGATGTACCCTAT
	tSLC4A1-R	AGCGAGGCAGGCGTGGATT
For virus		
HCV RNA	HCV-F	TGCTCATGGTGCACGGTCTAC
	HCV-R	TGCGGAACCGGTGAGTACAC
	HCV-P	FAM- CGCCCTATCAGGCAGTACCACAAGGCC -TRMRA

HCV_NS3	NS3-F	ACAGGGCACTTATAGGTAT
	NS3-R	CACTCACAAAGCACTACA
HCV_NS5B	NS5B-F	TTCGCATGGTCCTAATGACA
	NS5B-R	GTCAAGCCCGTGTAACCTCT
VSV	VSV-F	ACGGCGTACTTCCAGATGG
	VSV-R	CTCGGTTCAAGATCCAGGT

Forward (F) and reverse (R) primers were annotated by adding “-F” and “-R” in each primer name, respectively.

Supplementary Table S3. Antibodies used in this study.

Antibody name	Source	Application	Catalog number	Manufacturer
Primary antibody				
IFIH1/MDA5, RRID: AB_10734593	Rabbit polyclonal	WB (1:1000); IF-tissue (1:100)	21775-1-AP	Proteintech
PARP9, RRID: AB_2158929	Rabbit polyclonal	WB (1:1000); IF-tissue (1:100)	17535-1-AP	Proteintech
TRIM21, RRID: AB_3072944	Rabbit monoclonal	WB (1:2000)	HA721832	Huabio
Tubulin, RRID: AB_2827688	Rabbit polyclonal	WB (1:5000)	AF7011	Affinity Biosciences
Galectin-9/LGALS9, RRID: AB_2137233	Rabbit polyclonal	WB (1:1000)	17938-1-AP	Proteintech
GBP1, RRID: AB_2882457	Mouse monoclonal	WB (1:1000); IF-tissue (1:100)	67161-1-Ig	Proteintech
PKR/EIF2AK2, RRID: AB_2246451	Rabbit polyclonal	WB (1:1000)	18244-1-AP	Proteintech
USP18, RRID: AB_2772822	Rabbit polyclonal	WB (1:1000)	A16739	Abclonal
STING, RRID: AB_10665370	Rabbit polyclonal	IF-tissue (1:100)	19851-1-AP	Proteintech
CD81, RRID: AB_2766091	Rabbit polyclonal	WB (1:1000)	A5270	Abclonal
OCLN, RRID: AB_2737295	Rabbit polyclonal	WB (1:1000)	Ab216327	Abcam
CLDN1, RRID: AB_2881190	Rabbit polyclonal	WB (1:1000); IF-tissue (1:200)	28674-1-AP	Proteintech
β-Actin, RRID: AB_2687938	Mouse monoclonal	WB (1:10000)	66009-1-Ig	Proteintech
FOXO1, RRID: AB_10860103	Rabbit polyclonal	WB (1:1000)	18592-1-AP	Proteintech
Arginase-1/ARG1, RRID: AB_2800207	Rabbit monoclonal	WB (1:1000)	93668	Cell Signaling Technology
PCK1, RRID: AB_2160031	Rabbit polyclonal	WB (1:5000)	16754-1-AP	Proteintech
pAMPK (Thr172), RRID: AB_2834865	Rabbit polyclonal	WB (1:1000)	AF3423	Affinity Biosciences

pAKT (Ser473), RRID: AB_2315049	Rabbit monoclonal	WB (1:2000)	4060T	Cell Signaling Technology
GAPDH, RRID: AB_2107436	Mouse monoclonal	WB (1:10000)	60004-1-Ig	Proteintech
dsRNA (J2), RRID: AB_2936194	Mouse monoclonal	IF-tissue (1:500)	76651	Cell Signaling Technology
HCV NS3, RRID: AB_300673	Mouse monoclonal	WB (1:1000)	Ab13830	Abcam
HCV core, RRID: AB_325417	Mouse monoclonal	WB (1:1000)	MA1-080	Thermo Fisher Scientific
AHSP, RRID: AB_3718635	Rabbit polyclonal	IHC (1:300)	GB111822	Servicebio
GATA1, RRID: AB_3070489	Rabbit monoclonal	IF-tissue (1:200)	ET1704-41	Huabio
MPO, RRID: AB_2250866	Goat polyclonal	IF-tissue (1:200)	AF3667	R&D Systems
NE (Neutrophil Elastase), RRID: AB_2800136	Rabbit monoclonal	WB (1:1000)	89241T	Cell Signaling Technology
Histone H3 (citrulline R2 + R8 + R17), RRID: AB_3697176	Rabbit polyclonal	WB (1:1000); IF-tissue (1:100)	Ab281584	Abcam
Secondary antibody				
HRP conjugated anti-rabbit, RRID: AB_2811189	Goat	IHC (1:500)	GB23303	Servicebio
Alexa fluor® 488 conjugated anti-rabbit, RRID: AB_2340619	Donkey	IF-tissue (1:500)	711-546-152	Jackson ImmunoResearch
Alexa Fluor® 647 conjugated anti-rabbit, RRID: AB_2340625	Donkey	IF-tissue (1:500)	711-606-152	Jackson ImmunoResearch
Alexa Fluor® 647 conjugated anti-mouse, RRID: AB_2338902	Goat	IF-tissue (1:500)	115-605-003	Jackson ImmunoResearch
Alexa Fluor® 647 conjugated anti-goat, RRID: AB_2340438	Donkey	IF-tissue (1:500)	705-606-147	Jackson ImmunoResearch
HRP conjugated anti-rabbit, RRID: AB_2920567	Goat	WB (1:10000)	KP-5220-0458	Mandel Scientific
HRP conjugated anti-mouse, RRID: AB_2687537	Goat	WB (1:10000)	KP-5450-0011	Mandel Scientific

Supplementary Table S4. Marker genes of different cell types identified in tree shrew livers.

Genes were ranked by scores. Higher absolute value of score indicates lower P-value and higher expression. pct.1, percentage of cells where the gene is detected in the target cluster; pct.2: percentage of cells where the gene is detected, on average, in other clusters.

This table is presented as an Excel file.

Supplementary Table S5. Infection-associated DEGs between PBS-S and JFH1-S groups at 1 wpi.

This table is presented as an Excel file.

Supplementary Table S6. Marker genes of three neutrophil subclusters identified in tree shrew livers.

This table is presented as an Excel file.

Supplementary references

1. Xu J, Guo P, Hao S, et al. A spatiotemporal atlas of mouse liver homeostasis and regeneration. *Nat Genet*. 2024;56(5):953-969.
2. Liang Y, Kaneko K, Xin B, et al. Temporal analyses of postnatal liver development and maturation by single-cell transcriptomics. *Dev Cell*. 2022;57(3):398-414 e395.